







The Mass Density of Mg II Absorbers from the Australian Dark Energy Survey

ASIF ABBAS ¹, CHRISTOPHER W. CHURCHILL ¹, GLENN G. KACPRZAK ^{2,3}, CHRISTOPHER LIDMAN ^{4,5},
SUSANNA GUATELLI ^{6,7} AND SABINE BELLSTEDT ⁸

¹*Dept of Astronomy, New Mexico State University, Las Cruces, NM 88003, USA*

²*Centre for Astrophysics and Computing, Swinburne University, Victoria 3122, Australia*

³*ARC Centre of Excellence for All Sky Astrophysics in 3 Dimensions (ASTRO 3D), Australia*

⁴*Centre for Gravitational Astrophysics, College of Science, The Australian National University, ACT 2601, Australia*

⁵*The Research School of Astronomy and Astrophysics, Australian National University, ACT 2601, Australia*

⁶*University of Wollongong, Centre for Medical Radiation Physics, New South Wales, Australia*

⁷*Illawarra Health and Medical Research Institute, University of Wollongong, New South Wales, Australia*

⁸*ICRAR, University of Western Australia, 35 Stirling Highway, Crawley, WA 6009, Australia*

ABSTRACT

We present an all-southern sky survey for Mg II $\lambda\lambda 2796$, 2803 doublet absorbers in 951 $z < 4$ AGN/quasar spectra from the Australian Dark Energy Survey (OzDES). The spectral resolution ranges from $R = 1400$ – 1700 over the wavelengths 3700 – 8800 Å. The survey has a 5σ detection completeness of 50% and above for rest-frame equivalent widths $W_r(2796) \geq 0.3$ Å. We studied 656 Mg II absorption systems over the redshift range $0.33 \leq z \leq 2.19$ with equivalent widths $0.3 \leq W_r(2796) \leq 3.45$ Å. The equivalent width distribution is well fit by an exponential function with $W_* = 0.76 \pm 0.04$ Å and the redshift path density exhibits very little evolution. Overall, our findings are consistent with the large, predominantly northern-sky, surveys of Mg II absorbers. We developed and implemented a Monte Carlo model informed by a high-resolution Mg II survey for determining the Mg II mass density, Ω_{MgII} . We found $\Omega_{\text{MgII}} \sim 5 \times 10^{-7}$ with no evidence of evolution over a ~ 7 Gyr time span following Cosmic Noon. Incorporating measurements covering $2.0 \leq z \leq 6.4$ from the literature, we extended our insights into Mg II mass density evolution from the end of reionization well past the Cosmic Noon epoch. The presented Monte Carlo model has potential for advancing our knowledge of the evolution of mass densities of metal-ions common to quasar absorption line studies, as it exploits the efficiency of large low-resolution surveys while requiring only small samples from expensive high-resolution surveys.

Keywords: Quasar absorption line spectroscopy (1317) — Circumgalactic medium (1879)

1. INTRODUCTION

Characterizing the evolution of the gaseous properties of the universe is a key step to understanding the processes that shape the universe of galaxies and groups and clusters of galaxies (Tumlinson et al. 2017). These processes are also responsible for the build up of the chemical elements through what is often called the cosmic baryonic cycle (e.g., Péroux & Howk 2020). The study of cosmic gas between, surrounding, and embedded in galaxies is facilitated by the tool of quasar absorption-line spectroscopy.

Absorption from specific ionization states of different chemical elements probe and provide insight into various gaseous structures and environments in the universe. For example, absorption from five-times ionized oxygen (O VI) probes the hotter more diffuse regions of the universe (e.g., Cen & Ostriker 1999; Tripp et al. 2006; Oppenheimer & Davé 2009; Nelson et al. 2018; Bradley et al. 2022), whereas absorption from singly ionized magnesium (Mg II) probes the cooler denser regions nearer to galaxies (e.g., Bergeron & Boissé 1991; Steidel et al. 1994; Kacprzak et al. 2010;

Nielsen et al. 2013). Magnesium is an abundant α -process element resulting from Type-II supernovae, so it is a good tracer of gaseous environments that has been enriched by recent star formation (e.g., Lauroesch et al. 1996).

In first decades following the discovery of the cosmological nature of quasars (Schmidt 1963), Mg II $\lambda\lambda 2796$, 2803 resonant fine-structure absorption lines were found to be a common feature in their spectra (e.g., Kinman & Burbidge 1967; Carswell et al. 1975; Burbidge et al. 1977). Over the next decades, the statistical characteristics of this absorber population were slowly uncovered (e.g., Bergeron & Boisse 1984; Lanzetta et al. 1987; Tytler et al. 1987; Sargent et al. 1988; Caulet 1989; Steidel & Sargent 1992). In these early optical studies, the redshifted Mg II doublet was observable over the redshift range $0.3 \leq z \leq 2.2$. These works established that Mg II absorbers were cosmologically distributed and examined their redshift evolution, including their redshift path densities, redshift clustering, and equivalent width and doublet ratio distributions. They were mostly sensitive to absorbers with rest-frame equivalent widths $W_r \geq 0.3$ Å. The

higher-resolution survey of Petitjean & Bergeron (1990) was able to examine the kinematics and multi-component structure, and their velocity splitting and column density distributions.

With the advent of Sloan Digital Sky Survey (SDSS), successively larger optical low-resolution ground-based surveys were undertaken (e.g. Nestor et al. 2005; Lundgren et al. 2009; Seyffert et al. 2013; Zhu & Ménard 2013; Raghunathan et al. 2016), from which the statistics of the absorber characteristics were measured to high precision. The advent of optical high-resolution spectrographs on 10-meter class telescopes opened two new windows: (1) the sensitivity was improved such that the characteristics of absorbers with $W_r \leq 0.3 \text{ \AA}$ could also be studied (e.g., Churchill et al. 1999; Narayanan et al. 2007; Mathes et al. 2017), and (2) the kinematics and component structure of the absorbers could be studied (e.g., Churchill & Vogt 2001; Churchill et al. 2003; Prochter et al. 2006; Mshar et al. 2007; Churchill et al. 2020). And finally, the advent of sensitive infrared spectrographs on large telescopes allowed Mg II absorber studies to be extended up to $z \sim 7$ (e.g. Matejek et al. 2013; Chen et al. 2017; Codoreanu et al. 2017; Davies et al. 2023a; Sebastian et al. 2023). These moderately high-resolution spectra allowed analysis provided both the kinematics and the statistical characteristics of absorbers.

Though the characterization of the nature of Mg II absorbers has continually improved (see Churchill et al. 2024, for a brief summary), the cosmic evolution of the mass density of Mg II absorbing ions, Ω_{MgII} , is not well constrained across all redshifts over which Mg II has been studied. Recently, Sebastian et al. (2023) obtained robust measurements of Ω_{MgII} over the redshift range $2 \leq z \leq 6.5$ using the high-resolution X-shooter spectrograph (Vernet et al. 2011) on the Very Large Telescope. These measurements represent a significant improvement over the similar work by Codoreanu et al. (2017). However, measurements of Ω_{MgII} for the redshift range $0.3 \leq z \leq 2$ are only lower limits (Mathes et al. 2017). The reason they are lower limits is because the column densities were approximated using the apparent optical depth method, which is known to provide lower limits when absorption profiles exhibit unresolved saturation (Savage & Sembach 1991; Jenkins 1996).

Measuring Ω_{MgII} is challenging because it requires an accurate characterization of the Mg II column density distribution, and that requires Voigt profile fitting of Mg II absorbers in high-resolution spectroscopy. First, high resolution spectroscopy is expensive, requiring time on competitive 10-meter class telescopes. Second, there are only so many bright quasars suitable for high signal-to-noise high-resolution spectroscopy. Third, Voigt profile fitting complex absorption systems is time intensive work. These bottlenecks limit the sample sizes for accurately measuring Ω_{MgII} . To date, the SDSS has archived roughly 10^6 low-resolution quasar spectra containing roughly 10^5 Mg II absorbers (e.g., Raghunathan et al. 2016; Anand et al. 2021). We ask, is it plausible to develop a method to accurately estimate the column densi-

ties of these absorbers and exploit the existing huge archives to obtain high precision estimates Ω_{MgII} ?

As previously mentioned, for $2 \leq z \leq 7$ recent works (Codoreanu et al. 2017; Sebastian et al. 2023) have measured Ω_{MgII} using the X-shooter. Sebastian et al. (2023) found that Ω_{MgII} increases by a factor of 10 to 100 from $z \sim 7$ to $z \sim 2$. This suggests an increase in α -group elements in low-ionization gas structures in the epoch leading up to Cosmic Noon (e.g., Förster Schreiber & Wuyts 2020), when the universe is at its peak activity ($2 \leq z \leq 3$). On account that Mathes et al. (2017) measured lower limits on Ω_{MgII} for $z < 2$, the evolution of the mass density of Mg II absorbers following Cosmic Noon remains unknown.

In this paper, our main goals are to present a census of the Mg II absorbers in the OzDES quasar spectra database and to develop and pilot a method to better constrain Ω_{MgII} for $z < 2$ using low-resolution quasar spectra. In addition to providing deeper insight into the evolution of Mg II absorbers, we may be able to ultimately leverage the existing large archives of low-resolution spectra to obtain precision measurements of mass densities of commonly absorber populations, such as Mg II, Fe II, C IV, Si IV, etc. Our secondary goal is to conduct a blind and unbiased survey of Mg II absorbers exclusive to the southern hemisphere. For both goals, we use the archived low-resolution AGN/quasar spectra obtained through the Australian Dark Energy Survey (OzDES, Yuan et al. 2015; Childress et al. 2017; Lidman et al. 2020).

In Section 2, we present the AGN/quasar catalog and the data reduction. In Section 3, we detail the absorption lines survey methods, the detection algorithm, and assess the completeness of the algorithm. Section 4 presents the survey results, including the equivalent width distribution, and the path density of the absorption systems. We also provide a brief comparison to northern hemisphere studies. In Section 5, we introduce a Monte Carlo model to estimate the mass density of Mg II absorbers. In section 6, we compare higher redshift measurements and examine possible evolution in the mass density across the Cosmic Noon epoch. We conclude in Section 7. Throughout this paper, we adopt $\Omega_M = 0.321$, $\Omega_\Lambda = 0.679$ and $H_0 = 71.9 \text{ km s}^{-1} \text{ Mpc}^{-1}$ from the Planck Collaboration (2020).

2. DATA AND DATA REDUCTION

The Dark Energy Survey (DES, Flaugher 2005) is a ground-based optical and near infrared survey designed to improve our understanding of the accelerating expansion of the universe and the nature of dark energy. The Australian Dark Energy Survey (OzDES, Yuan et al. 2015; Childress et al. 2017; Lidman et al. 2020) is a ground-based optical survey and is the primary source of galaxy/AGN spectroscopy for DES.

2.1. Australian Dark Energy Survey

The OzDES survey used the 2-degree field (2dF) fiber positioner and the AAOmega spectrograph (Sharp et al. 2006) on the 3.9-meter Anglo-Australian Telescope (AAT). OzDES targeted 10 deep fields in the DES supernova survey over 6

years to obtain the redshifts of thousands of galaxies. OzDES ran 6 observing seasons from 2013 to 2019, with two extra deep fields, C3 and X3, receiving the highest priority, followed by two E fields, E1 and E2. These fields were observed repeatedly enabling redshifts to be obtained for faint sources. Of all the sources observed, AGN received a quarter of the total fiber hours allotted to OzDES.

The AGN/quasars selected for observation were in the redshift interval $0 < z < 4$. The 951 AGN/quasars were monitored with the goal of measuring the lags between the continuum from the accretion disk and the broad lines from the broad line emission regions (e.g., Yu et al. 2021, 2023; Penton et al. 2022; Malik et al. 2023). The AGN were observed with the x5700 dichroic, resulting in a spectral range from 3700 Å to 8800 Å at a resolution ranging from $R = 1400$ –1700.

2.2. Data Reduction/Calibration

All OzDES quasar spectra were processed through an upgraded version of the analysis package `2dfdr` (Croom et al. 2004). As described in more detail in Yuan et al. (2015) and Childress et al. (2017), these steps include (1) overscan and bias subtraction, bad pixel masking, and preliminary cosmic ray removal, (2) tram line mapping, i.e., locating fiber traces, (3) spectral extraction, (4) wavelength calibration in units of constant wavelength, (5) sky subtraction using extracted sky fibers and a principle component analysis to remove sky line residuals, and (6) combining and splicing, which involves co-addition of multiple frames and cosmic ray removal. The OzDES spectra are resampled to a common wavelength grid. This is done when the spectra from the red and blue arms of the spectrograph are combined. The redshifts of the quasars were determined by interactive software and visual inspected by OzDES team members using the interactive redshifting software RUNZ.

In Figure 1, we show the median signal-to-noise ratio (SNR), in 200 Å bins, from 3700 Å to 8900 Å for all 951 OzDES quasar spectra. The median SNR is less than 25 below 4200 Å, making it difficult to reliably identify MgII absorption lines below $z \simeq 0.43$. Therefore, we limit our search for absorption lines to above 4200 Å. We further restrict our search for MgII $\lambda\lambda 2796, 2803$ doublets redward of the Ly α line in order to avoid confusion in the Ly α forest.

In Figure 2, we show a typical quasar spectrum from the OzDES survey. This quasar resides at $z \sim 2.41$. There are three intervening MgII absorbers detected in the spectrum. The continuum fit is given by the orange curve.

2.3. Continuum Fitting

To estimate the continuum for each spectrum, we employ a three-step process. In Step 1, we approximate the continuum at a pixel j as the median flux in a window centered around the pixel j . However, the median continuum is not accurate across absorption and emission lines. For Step 2, we identify all statistically significant (greater than 3σ) absorption features using the methods described in Lanzetta et al. (1987). In Step 3, we replace the continuum across absorp-

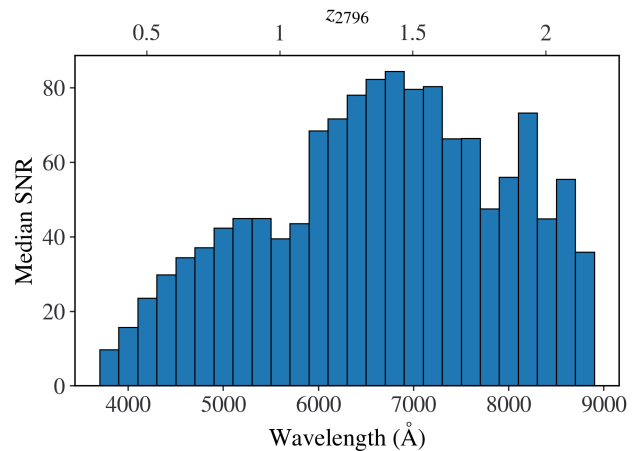


Figure 1. A histogram of the median signal-to-noise ratio (SNR) of the 951 OzDES quasar spectra in 200 Å bins. (lower axis) SNR as a function of wavelength covering the spectral range of the spectra, 3700 to 8900 Å. (top axis) SNR as a function of the redshift for the MgII $\lambda 2796$ line. The dip at 5700 Å ($z_{2796} \sim 1$) is due to the x5700 dichroic.

tion and emission lines with Legendre polynomial fits using the method outlined in Sembach & Savage (1992). In this step, the absorption features are masked from the fits. This process rectifies the systematic errors present in the median continuum and provides a formal framework for accounting for uncertainties due to the estimated continuum flux across absorption lines (see 2.3.3). In the following subsections we detail the continuum fitting.

2.3.1. Step 1: Median Continuum

For computing the median flux, we adopt a 50-pixel wide window centered on a pixel j . The median centered on pixel j is repeated for pixels $j + 1$, $j + 2$ and so forth. At the blue end and red ends of the spectrum, we adopt the median computed for the last pixels for which the full 50-pixel window can be employed. As illustrated in Figure 3(a), the median tends to be underestimate the continuum across absorption features. We thus need to refine the continuum estimate across the absorption features.

2.3.2. Step 2: Feature Masking for Refinement

In order to refine the continuum estimate across absorption features, we first build a catalog of the absorption features. Then, as described in Section 2.3.3, we mask the pixels comprising the features and refine the continuum fit. At this stage in our analysis, these absorption features are not used for identifying MgII doublets; they are used only for pixel masking and continuum fit refinement.

To locate the features, we use a slightly modified version of the “aperture method” as formulated by Lanzetta et al. (1987). This method compares the equivalent width computed over a fixed number of pixels (the aperture) to its uncertainty and identifies spectral regions where the equivalent width in an aperture is significant.

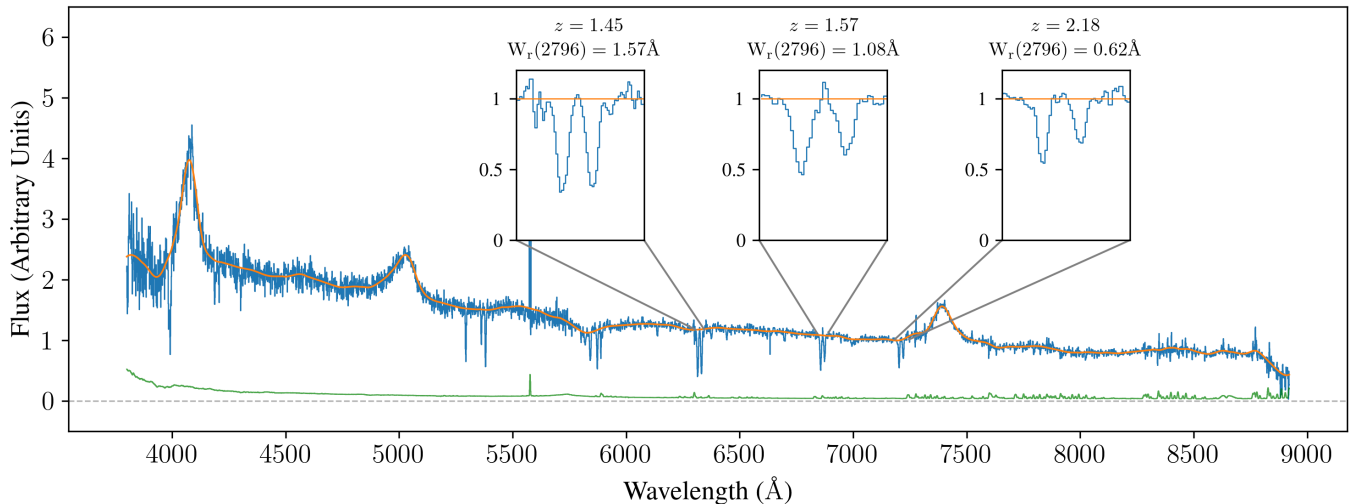


Figure 2. OzDES spectrum of the quasar SVA1-COADD-2925403880 ($z \sim 2.41$) showing the continuum model (orange) and the sigma spectrum (green). Three intervening MgII absorbers are highlighted (insets) at absorption redshifts $z = 1.45$, ($\sim 6300 \text{ \AA}$), $z = 1.57$, ($\sim 6850 \text{ \AA}$), and $z = 2.18$, ($\sim 7200 \text{ \AA}$).

We define the equivalent width of pixel j as $w_j = D_j \Delta \lambda_j$, where $D_j = 1 - f_j/f_j^c$ is the flux decrement in the pixel, and where $\Delta \lambda_j = \lambda_{j+1} - \lambda_j$. The quantity f_j is the flux density and f_j^c is the estimated continuum at pixel j from Step 1. The uncertainty in the equivalent width per pixel is $\sigma_{w_j} = \sigma_{D_j} \Delta \lambda_j$. At this stage, we assume no uncertainty in the continuum estimate, so that $\sigma_{D_j} = |\sigma_{f_j}|$.

To identify candidate features, we scan the spectrum from blue to red for the condition $w_j/\sigma_{w_j} \geq 3$, which we deem a significant equivalent width for pixel j . We then search for the blueward and redward extremes of the candidate absorption feature by scanning the spectrum blueward and redward of pixel j for the first pixel satisfying the condition $w_j/\sigma_{w_j} \geq 1$. This yields pixel j^- for the blue extreme of the feature and pixel j^+ for the red extreme of the feature. The region from pixel j^- to pixel j^+ comprises the aperture over which the candidate feature is masked from the refinement to the continuum fit.

2.3.3. Step 3: Legendre Polynomial Fit

The existing median continuum spanning an absorption feature is replaced with a Legendre polynomial fit. To ensure a robust fit, the first 150 “clean pixels” (pixels devoid of statistically significant absorption) on both sides of a feature are included in the fit. This step yields a refined continuum across absorption features.

Following Sembach & Savage (1992), we adopt Legendre polynomials due to their orthonormal properties. Being orthogonal, the fitted coefficients for each order of the polynomial are independent of one another, which has the added property that the uncertainties in the coefficients are also independent (the covariance matrix is diagonal). As we show below, this allows us to objectively determine the most optimal order, m , of the fitted polynomial.

A Legendre polynomial of order m is written

$$P_m(x) = \sum_{k=0}^m a_k P_k(x). \quad (1)$$

where $P_0(x) = 1$, $P_1(x) = x$, and

$$P_k(x) = [(2k-1)xP_{k-1}(x) - (k-1)P_{k-2}(x)]/k, \quad (2)$$

for $k \geq 2$, where k is the index of each term of the polynomial. To enable the orthonormal properties, for each pixel j the $P_k(x_j)$ are defined over the range $x_j \in [-1, +1]$, where we adopt the definition $x_j = (\lambda_j - \bar{\lambda})/\delta\lambda$, where λ_j is the wavelength at pixel j , and where $\bar{\lambda} = (\lambda_+ + \lambda_-)/2$ and $\delta\lambda = (\lambda_+ - \lambda_-)/2$ for the 300 pixel interval over which $\lambda_- \leq \lambda_j \leq \lambda_+$, with λ_- and λ_+ being the starting and ending wavelengths of the pixel interval.

We adopt modified χ^2 least-squares minimization technique, where

$$\chi_m^2 = \sum_{j=1}^{n_{\text{pix}}} \frac{(f_j(x_j) - P_m(x_j))^2}{\sigma_{f_j}^2(x_j)}, \quad (3)$$

for order m where $f_j(x_j)$ is the flux at pixel j , $P_m(x_j)$ is the value of the fitted Legendre polynomial of order m evaluated at pixel j , and $\sigma_{f_j}(x_j)$ is the uncertainty in the flux at pixel x_j , and n_{pix} is the number of pixels in the fitted interval of the spectrum. For the least-squares fitting, we use the LEGFIT¹ function from the NumPy module. This function returns both the coefficients and the sum of squared residuals of the least squares fit.

The lower the order, m , the fewer the fitting coefficients and the smaller the formal error in the continuum fit, $P_m(x_j)$.

¹ numpy.polynomial.legendre.legfit (NumPy v1.26 Manual).

Thus, it is desirable to use the smallest order polynomial that provides a statistically significant improvement in the refinement of the continuum. The orthonormal properties of Legendre polynomials provides the desirable property that adding or removing the highest-order term from the fit does not impact the fitted values of the fitting coefficients for the other lower-order terms.

We use the F -test to determine the optimal order of the fit. By optimal, we mean the minimum m required to provide a statistically robust fit in that adding an additional order does not statistically improve the χ^2 statistic. We aim to obtain the most statistically significant fit while minimising the formal error in the fit. The F -test statistic for comparing the fit of order m to order $m - 1$ is

$$F_m = \frac{\chi_{m-1}^2 - \chi_m^2}{\chi_m^2 / \nu_m}, \quad (4)$$

where $\nu_m = n_{\text{pix}} - m - 1$ is the number of degrees of freedom for a fit of order m applied to n_{pix} .

An additional term is retained only if the probability (p -value) that obtaining F_m greater than the measured value is smaller than a specified value, which is $p = 1 - \text{CL}$, where CL is the double-sided confidence level. The p -value is then computed using the regularized incomplete beta function,

$$p = 2 \frac{\Gamma(a+b)}{\Gamma(a)\Gamma(b)} \int_0^x t^{a-1} (1-t)^{b-1} dt, \quad (5)$$

where $a = \nu_m/2$, $b = \nu_{m-1}/2$, and where $x = \nu_m / (\nu_m + \nu_{m-1} F_m)$. We adopt a confidence level of 95%, so that an additional term is only retained in the fit when $p < 0.05$. That is, when a term corresponding to order $m + 1$ is added and $p \geq 0.05$, that term is rejected and we adopt order m . Almost all of the polynomial fits are of the order 4–6.

Once the order is determined, we can compute the uncertainty in the continuum fitted value at pixel j from

$$\sigma_{f_j^c}^2(x_j) = \sum_{i=0}^m \sum_{k=0}^m \sigma_{a_{ik}}^2 P_j(x_j) P_k(x_j). \quad (6)$$

where $\sigma_{a_{ik}}^2$ are in the uncertainties in the fitted coefficients obtained from the diagonal of the covariance matrix. Though the corresponding wavelength at pixel j can be computed from

$$\lambda_j = x_j \delta\lambda + \bar{\lambda} = [\lambda_+(1+x_j) + \lambda_-(1-x_j)]/2, \quad (7)$$

pixel index j immediately provides the wavelength λ_j corresponding to x_j . Further details of the applications of Legendre polynomials and the F -test can be obtained in Appendix 1.1 of Sembach & Savage (1992).

In Figure 3, we show the continuum estimation across a Mg II $\lambda\lambda 2796, 2803$ doublet with the aperture defined by the red vertical dashed lines. Figure 3(a) illustrates the dip in the continuum when using the median flux for estimation (Step 1). In Figure 3(b), following Steps 2 and 3, we show the

final adopted continuum normalized spectral region. The depression has been corrected by applying a 9th order Legendre polynomial fit to 150 “clean” pixels on each side of the Mg II doublet (those between the green vertical lines, omitting those between the orange and red lines). The optimal order of the polynomial was estimated through the F -Test given in Eq. 4.

3. THE SURVEY

In this section, we describe how we define our detection threshold sensitivity, how we objectively survey for and define candidate Mg II doublets, and how we evaluate the completeness of our survey for these absorption lines.

3.1. The Detection Threshold

The aperture method utilized in Section 2.3.2 is suitable for locating strong absorption features for the purpose of refining the continuum model; however, it lacks sensitivity for detecting weak, unresolved absorption lines. Thus, for objectively finding Mg II doublets, we adopt the optimized method of Schneider et al. (1993), which employs weighting of the instrumental line spread function (ISF) to maximize the detection sensitivity for absorption. This optimized method is applied following the refinement of the continuum model using the Legendre polynomials.

We modeled the ISF as a Gaussian function with root-mean square width (Gaussian standard deviation)

$$\sigma_j = \frac{\lambda_j}{2\sqrt{2 \ln(2)} R}, \quad (8)$$

centered on pixel j using the discretized expression with index n

$$\mathcal{P}_n = \frac{\exp(-y_{kj}^2)}{\sum_{n=1}^N \exp(-y_{kj}^2)}, \quad (9)$$

where

$$y_{kj} = \frac{\lambda_j - \lambda_k}{\sigma_j}, \quad (10)$$

and where $N = 2J_0 + 1$ is the number of pixels spanning the ISF, where $J_0 = 2p$ with $p = 3$ being the number of pixels per resolution element, which yields $N = 13$. The convolution index at pixel j is $k = j + (n - 1) - J_0$, which is a function of the ISF index n . The resolution ranges from $R = 1400$ in the blue to $R = 1700$ in the red. We assumed a linear progression over the wavelength range 3700 to 8900 Å, yielding $R = 1400 + 0.058(\lambda_j - 3700)$.

The ISF weighted equivalent width per resolution element centered on pixel j is

$$w_j = \frac{\Delta\lambda_j}{\mathcal{P}^2} \sum_{n=1}^N \mathcal{P}_n D_k, \quad \mathcal{P}^2 = \sum_{n=1}^N \mathcal{P}_n^2, \quad (11)$$

where D_k is the flux decrement defined in Section 2.3.2, and $\Delta\lambda_j$ is the width of pixel j . The uncertainty in w_j is the 1σ limiting equivalent width detection threshold sensitivity

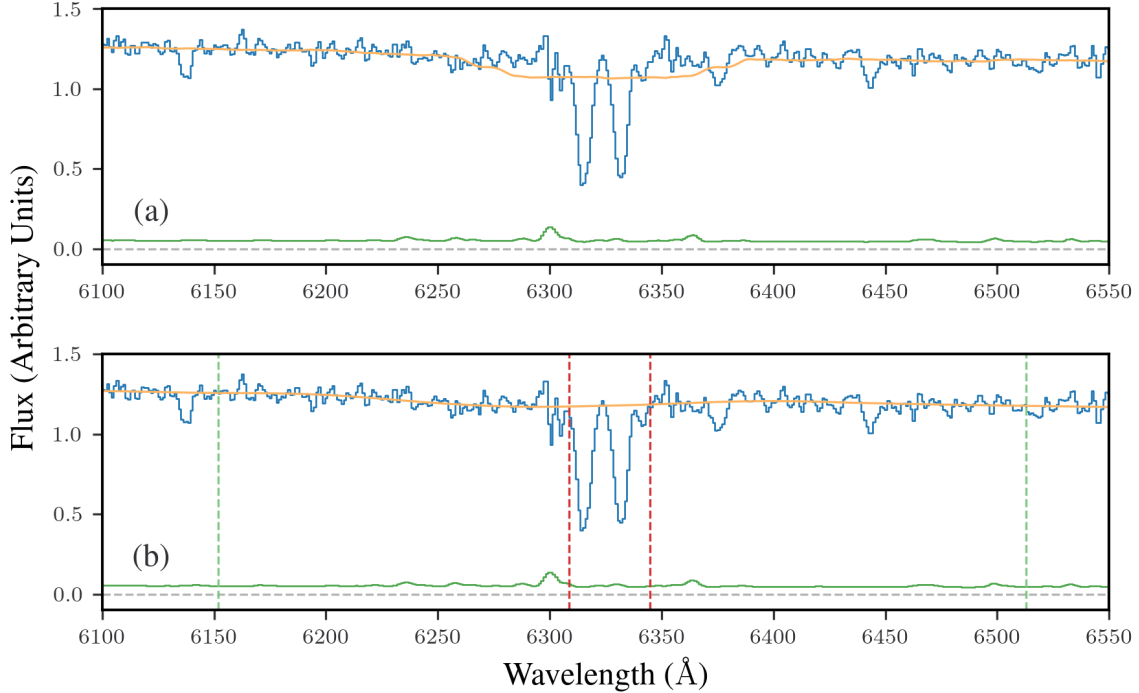


Figure 3. Expanded region highlighting the $z = 1.45$ MgII absorber in the SVA1-COADD-2925403880 spectrum. (a) The continuum estimated (orange curve) using the median continuum method described in Section 2.3.1. The sigma spectrum is shown in green. The absorption feature causes an underestimation in the local continuum. (b) The feature is objectively identified and its aperture (vertical red lines) is determined using the aperture method described in Section 2.3.2. A region spanning ± 150 pixels is defined (vertical green lines) across which a Legendre polynomial fit is applied as described in Section 2.3.3.

per resolution element centered at pixel j in a given quasar spectrum; it is written

$$\sigma_{w_j} = \frac{\Delta\lambda_j}{\mathcal{P}^2} \left(\sum_{n=1}^N \mathcal{P}_n^2 \sigma_{D_k}^2 \right)^{1/2}. \quad (12)$$

The uncertainty in the flux decrement,

$$\sigma_{D_k}^2 = \left[\frac{f_k}{f_k^c} \right]^2 \left(\left[\frac{\sigma_{f_k}}{f_k} \right]^2 + \left[\frac{\sigma_{f_k^c}}{f_k^c} \right]^2 \right) \quad (13)$$

includes the uncertainty in the continuum model.

In spectral regions where we have refined the continuum estimate around absorption features using the Legendre polynomial fits, we have $f_k^c = P_m(\lambda_k)$ given by Eq. 1 and $\sigma_{f_k^c}$ given by Eq. 6. As we have adopted the lowest order m that provides a statistically significant refinement in the continuum, we have minimized $\sigma_{f_k^c}$ and thus maximized our detection sensitivity, σ_{w_j} , while properly accounting for uncertainty in the continuum estimate (see Eqs. 3, 4, and 5). Note that a smaller value of σ_{w_j} translates to a smaller (more sensitive) equivalent width detection threshold. In spectral regions where we did not refine the original continuum estimate, which was based on the median method described in Section 2.3.1, we adopt $\sigma_{f_k^c} = 0.4\sigma_{f_k}$, based on the findings of Sembach & Savage (1992) and Churchill et al. (2015).

3.2. Locating Candidate Doublets

Absorption features are objectively identified by scanning each spectrum pixel by pixel searching for the condition $w_j > N_\sigma \sigma_{w_j}$, where we adopt $N_\sigma = 5$. In other words, when the equivalent width per resolution element centered on pixel j exceeds or equals N_σ times its uncertainty, we consider this to be, at a minimum, a detection of unresolved absorption. Having identified this pixel, we then search blueward to determine j_- corresponding to the pixel with the first occurrence of $w_j \leq \sigma_{w_j}$ and redward to determine j_+ , the pixel corresponding to the first occurrence of $w_j \leq \sigma_{w_j}$. This provides the detection aperture of the absorption feature.

We next aim to ascertain if this absorption feature is plausibly one member of a MgII doublet or comprises both members of a partially blended MgII doublet. Within the aperture from j_- to j_+ , we first locate the number of minima in w_j and their pixel locations. For candidate testing, if there is a single minimum we assume this absorption feature corresponds to a MgII $\lambda 2796$ line centered on the wavelength corresponding to the pixel of the minimum w_j . We then locate the pixel, j' , corresponding to the wavelength of the $\lambda 2803$ member of the doublet and determine if the condition $w_j/\sigma_{w_j} > 3$ is met for any of the pixels $j = j' - 1, j', j' + 1$. If the condition is met, we then determine j'_- and j'_+ for the $\lambda 2803$ candidate and check that $j'_- \geq j_+$. If that latter condition is not met, then we merge the aperture for the two candi-

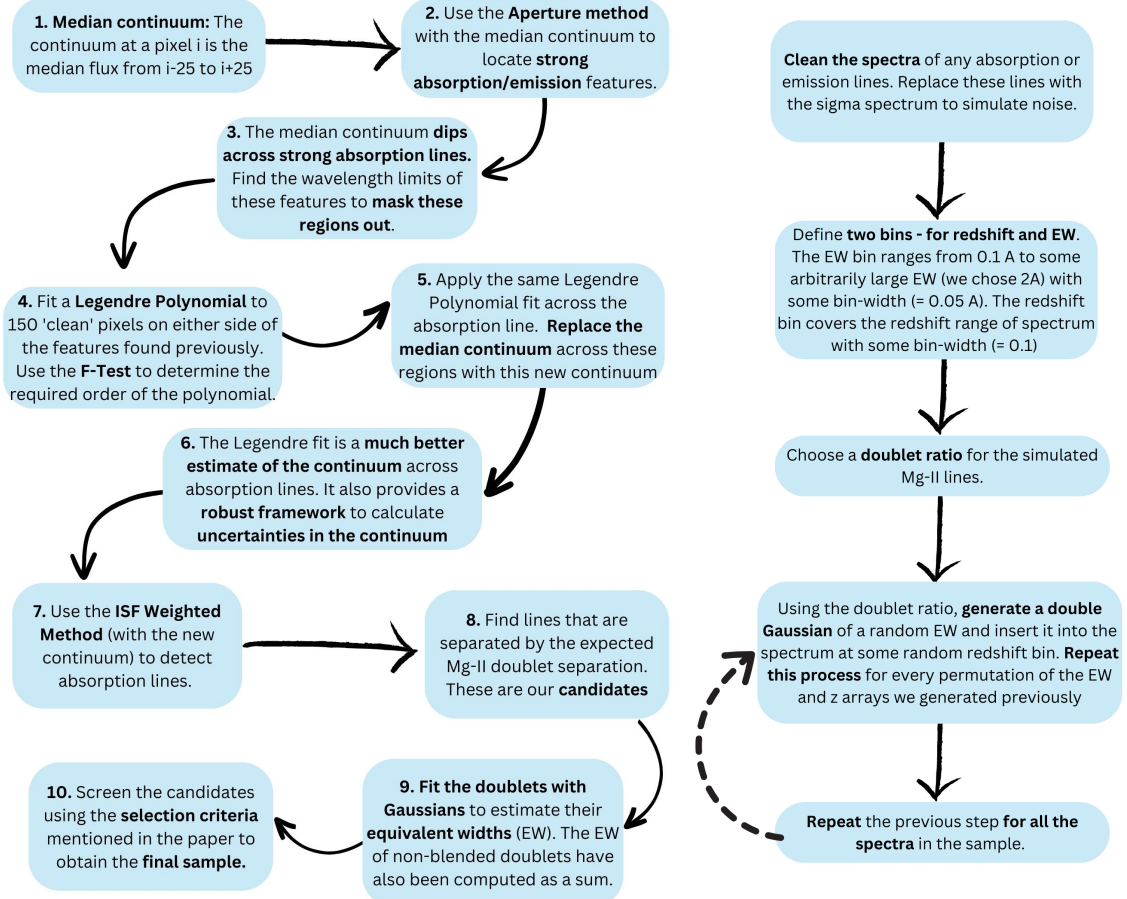


Figure 4. (left) Schematic flowchart summarizing the MgII doublet detection algorithm (Sections 2.3 through 3.1), from modeling the continuum to computing the equivalent width. (right) Schematic flowchart of the steps for computing the completeness function (see Section 3.3) of the detection algorithm. The values in the parentheses can be altered as required.

date lines into a single aperture covering both lines, meaning we adopt pixel j_- for the blue extremity and adopt pixel j_+ for the red extremity.

To measure the line centers and equivalent widths of the candidate double absorption lines, we simultaneously fit the two lines using a two-component Gaussian function of the form

$$f(\lambda) = \sum_{i=1}^2 A_i \exp \left\{ -\frac{(\lambda - \lambda_{c,i})^2}{2\Sigma_i^2} \right\}, \quad (14)$$

where we denote $i = 1$ for the $\lambda 2796$ transition and $i = 2$ for the $\lambda 2803$ transition, and where A_i is the component amplitude, $\lambda_{c,i}$ is the component central wavelength, and Σ_i is the line root-mean square width of the component. The fitting was performed using LMFIT (Newville et al. 2014), a non-linear least square minimization curve-fitting package. If a component was fitted with a width smaller than the ISF width, given by Eq. 8, then the component width was frozen at the ISF width and the minimization was repeated to obtain the component amplitude and central wavelength. The

LMFIT package also yields the uncertainties in the fitted parameters, σ_{A_i} , $\sigma_{\lambda_{c,i}}$, and σ_{Σ_i} .

The equivalent width of the each component is computed from the fitted parameters by integrating across the component, which yields,

$$W_i = \sqrt{2\pi} A_i \Sigma_i \quad (15)$$

with fractional uncertainty

$$\frac{\sigma_{W_i}}{W_i} = \left[\left(\frac{\sigma_{A_i}}{A_i} \right)^2 + \left(\frac{\sigma_{\Sigma_i}}{\Sigma_i} \right)^2 - 2 \frac{\sigma_{A_i} \sigma_{\Sigma_i}}{A_i \Sigma_i} \right]^{1/2}. \quad (16)$$

To confirm a MgII doublet candidate, we then apply two tests. First, we examine if the members of the candidate doublet are at a consistent redshift by applying the criterion $|z_1 - z_2| \leq \sigma_z$, where $z_1 = \lambda_{c,1}/\lambda_1 - 1$, $z_2 = \lambda_{c,2}/\lambda_2 - 1$, where λ_1 and λ_2 are the respective rest-frame wavelengths of the $\lambda 2796$ and $\lambda 2803$ transitions, and where the variance in the quantity $|z_1 - z_2|$ is

$$\sigma_z^2 = \left[\frac{\sigma_{\lambda_{c,1}}}{\lambda_1} \right]^2 + \left[\frac{\sigma_{\lambda_{c,2}}}{\lambda_2} \right]^2. \quad (17)$$

Second, we test if the doublet ratio, $DR = W_1/W_2$, is consistent with the physically allowed range using the condition

$$(1 - \sigma_{DR}) \leq DR \leq (2 + \sigma_{DR}), \quad (18)$$

where

$$\sigma_{DR}^2 = DR^2 \left(\left[\frac{\sigma_{W_1}}{W_1} \right]^2 + \left[\frac{\sigma_{W_2}}{W_2} \right]^2 \right) \quad (19)$$

is the uncertainty in DR , which, on average is 0.24. The average uncertainty in DR is 0.24. If both conditions are satisfied, we consider the two lines to be a candidate doublet and save the absorption properties for further vetting and processing. We simply define the absorption redshift as $z_{\text{abs}} = z_1$.

If, during our search for the number of minimum in w_j within the aperture from j_- to j_+ , we locate two minima, we deblended the absorption feature using two-component Gaussian decomposition. We then compute the equivalent widths and their uncertainties, and perform the two checks for a consistent redshift for the fitted line centers and a physically consistent doublet ratio. If both conditions are satisfied, we assign $z_{\text{abs}} = z_1$ and save the absorption properties for further vetting and processing. In the left panels of Figure 4, we present a schematic flowchart of the detection algorithm and candidate doublet testing.

3.3. Completeness of the Detection Algorithm

We assessed our detection algorithm using a Monte Carlo simulation to compute the completeness function

$$C(W_r, DR, z) = \frac{n_{\text{det}}}{n}, \quad (20)$$

which we define as the fraction of systems we successfully detect as a function of MgII $\lambda 2796$ rest-frame equivalent width, MgII $\lambda \lambda 2796, 2803$ doublet ratio, and redshift. In Eq. 20, n is the total number of known doublets with MgII $\lambda 2796$ rest-frame equivalent width W_r , doublet ratio DR , and redshift z , and n_{det} is the number of those detected.

In the right-hand panel of Figure 4, we present a schematic of the steps to compute the completeness function. First, we “clean” the OzDES spectra of all absorption lines redward of the Ly α emission line. That is, the flux values in pixels associated with absorption features objectively located at the $N_\sigma = 3$ level (as described in Section 3.2) were replaced with the fitted continuum flux. These replacement continuum values were given simulated Gaussian noise characteristics matching those of the continuum local to the replaced pixels. We then ran our detection algorithm on all cleaned quasar spectra to verify that no absorption lines were detected at the $N_\sigma = 3$ level.

To construct the completeness function, we defined a grid of redshift and equivalent width bins. We chose a bin width of $\Delta z = 0.1$ covering the domain of the survey redshift, $z \in (0.3, 2.2)$. We also chose W_r bin widths of $\Delta W_r = 0.1 \text{ \AA}$ over the domain $W_r \in (0.1, 4.0) \text{ \AA}$. For a given cleaned

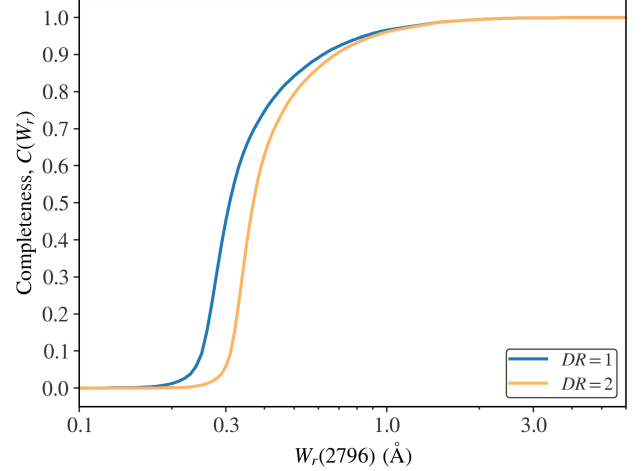


Figure 5. The completeness function $C(W_r, z)$ for $0.3 \leq z \leq 1.26$, for the MgII doublet detection algorithm describe in Section 3.3. The blue curve is for $DR = 1$ absorbers. The orange curve is for $DR = 2$ absorbers. The completeness is $\sim 50\%$ for $W_r = 0.3 \text{ \AA}$.

quasar spectrum, the completeness function is built up by stepping through the redshift and equivalent width bins. For a given (W_r, z) bin, we generated a mock MgII doublet pair using a double Gaussian function (see Eq. 14). First, we generated a uniform random deviate $A_1 \in (0, 1)$, which represents the flux decrement in the center of the $\lambda 2796$ line. Using Eq. 15, we computed the Gaussian line width, $\Sigma = W_1/(\sqrt{2\pi}A_1)$, where $W_1 = W_r(1+z)$ is the observed wavelength of the $\lambda 2796$ line. If $\Sigma < \sigma_j$, where σ_j is the ISF Gaussian standard deviation given by Eq. 8 evaluated at $\lambda_j = 2796.352(1+z)$, we set $\Sigma = \sigma_j$. This ensured that no mock lines are narrower than the instrumental resolution. We assumed both lines of the doublet experience the same line broadening, and therefore have the same Σ . We then generated a random deviate $DR \in (1, 2)$, and determined the flux decrement of the $\lambda 2803$ line, $A_2 = A_1/DR$. This yields $W_2 = \sqrt{2\pi}A_2\Sigma = \sqrt{2\pi}A_1\Sigma/DR = W_1/DR$.

Given $A_1, A_2, \Sigma, \lambda_{c,1} = 2796.352(1+z)$, and $\lambda_{c,2} = 2803.531(1+z)$, we used Eq. 14 to generate a MgII absorption doublet and inserted it into the cleaned spectrum. We then ran our detection algorithm and implement our doublet candidate criteria tests. This was done blind to the known redshift of the mock doublet. To account for the range of doublet ratios, for each (W_r, z) bin we generated, inserted, and tested 10 doublets with random $DR \in (1, 2)$. After all (W_r, z) bins were implemented for a given cleaned quasar, we stepped to the next cleaned quasar in the sample until all quasars were included. We then computed $C(W_r, DR, z)$ from Eq. 20.

The expectation is that a higher percentage of doublets with $DR \simeq 1$ will be detected compared to those with $DR \simeq 2$ because of the stronger absorption in the $\lambda 2803$ line. To examine this quantitatively, we undertook the calculation of $C(W_r, 1, z)$, holding $DR = 1$, and the calculation

Table 1. OzDES MgII Absorber catalog

OzDES Quasar ID [†]	z_{abs}	Wavelength (Å)	$W_r(2796)$ (Å)	$W_r(2803)$ (Å)
2925344837	0.602	4480.02	1.12±0.12	0.72±0.11
2925352689	1.228	6229.65	0.38±0.10	0.43±0.10
	1.663	7447.96	0.35±0.06	0.19±0.06
2925358447	0.756	4911.72	1.14±0.14	0.70±0.12
	0.840	5145.21	1.48±0.13	0.89±0.12
	0.889	5282.71	1.02±0.11	0.81±0.11
2925360137	0.759	4918.47	1.61±0.40	1.05±0.33
	0.937	5416.58	0.78±0.21	0.63±0.17
	1.224	6217.72	0.41±0.13	0.60±0.18
2925362319	1.652	7414.75	0.31±0.06	0.22±0.05

[†]OzDES identifiers have the prefix SVA1-COADD

NOTE—Table 1 is published in its entirety in machine-readable format. A portion is shown here for guidance regarding its form and content.

of $C(W_r, 2, z)$, holding $DR = 2$. In Figure 5, we show the detection completeness for $DR = 1$ and $DR = 2$ over the redshift range $0.3 \leq z \leq 2.2$. There is a clear drop in the detection completeness for small equivalent widths, with 50% completeness occurring at $W_r = 0.3$ Å.

3.4. The Absorber Sample

We found 717 MgII doublets over the redshift range $0.33 \leq z \leq 2.19$ with equivalent widths in the range $0.1 \leq W_r \leq 3.45$ Å. In Table 1 we present a partial list of the sample. In Figure 6, we show the distribution of rest-frame equivalent widths of the MgII $\lambda 2796$ transition versus redshift for the full catalog.

The detection completeness is 50% at $W_r = 0.3$. We adopt this minimum equivalent width threshold or our science sample. The science sample comprises all system above the horizontal dashed red line in Figure 6. The science sample is has 656 systems over the redshift range $0.33 \leq z \leq 2.19$ with equivalent widths in the range $0.3 \leq W_r(2796) \leq 3.45$ Å.

3.5. OzDES Redshift Path

The redshift path sensitivity function, $g(W, z)$, provides the number of quasar spectra in the survey in which a MgII absorption system with rest-frame equivalent width W_r or greater could be detected at redshift z . Following Lanzetta et al. (1987) and Steidel & Sargent (1992), this function is computed as sum over all N quasars in the sample

$$g(W_r, z) = \sum_{q=1}^N H(\Delta z_l) H(\Delta z_u) H(W_r - N_\sigma \sigma_{w_r}), \quad (21)$$

where $H(x)$ is the Heaviside function, $\Delta z_l = z - z_q^{\text{min}}$ and $\Delta z_u = z_q^{\text{max}} - z$, where z_q^{max} and z_q^{min} refer to the maximum and minimum redshifts adopted for the q th quasar spectrum, and where $\sigma_{w_r} = \sigma_w / (1 + z)$ is the rest-frame limiting

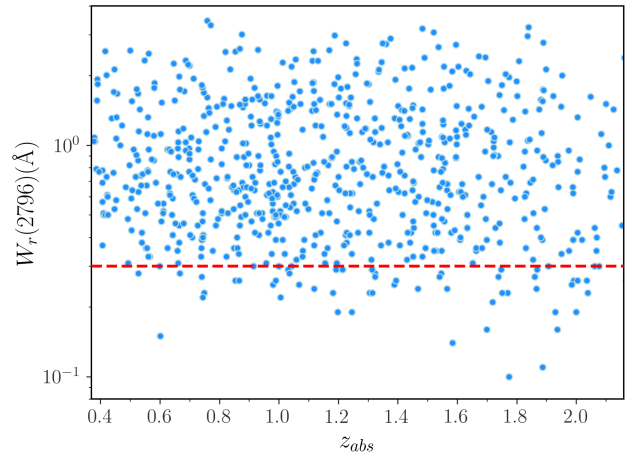


Figure 6. The rest-frame equivalent width of the MgII $\lambda 2796$ transition versus redshift for the full OzDES MgII absorber catalog of 717 absorbers. The red dashed horizontal line is $W_r = 0.3$ Å, corresponds to 50% completeness. Absorbers above line comprise our science sample of 656 absorbers.

equivalent width detection threshold at redshift z in spectrum q , where σ_w is given by Eq. 12. We adopted $N_\sigma = 5$. We avoid searching through the Ly α forest by adopting $z_q^{\text{min}} = 1215.67(1 + z_q)$ when the quasar Ly α emission line falls redward of 4200 Å, corresponding to the lower limit of our survey. We also limit our survey to $cz_q^{\text{max}} = -5000$ km s⁻¹ from the MgII emission of the quasar (see, for example, Weymann et al. 1981).

In Figure 7, we present a “heatmap” showing the number of quasar spectra in which a MgII absorber at a redshift z with a rest-frame equivalent width W_r or greater could have been detected. The spectrograph used for the survey, AAOmega, consists of red and blue arms that are split by a

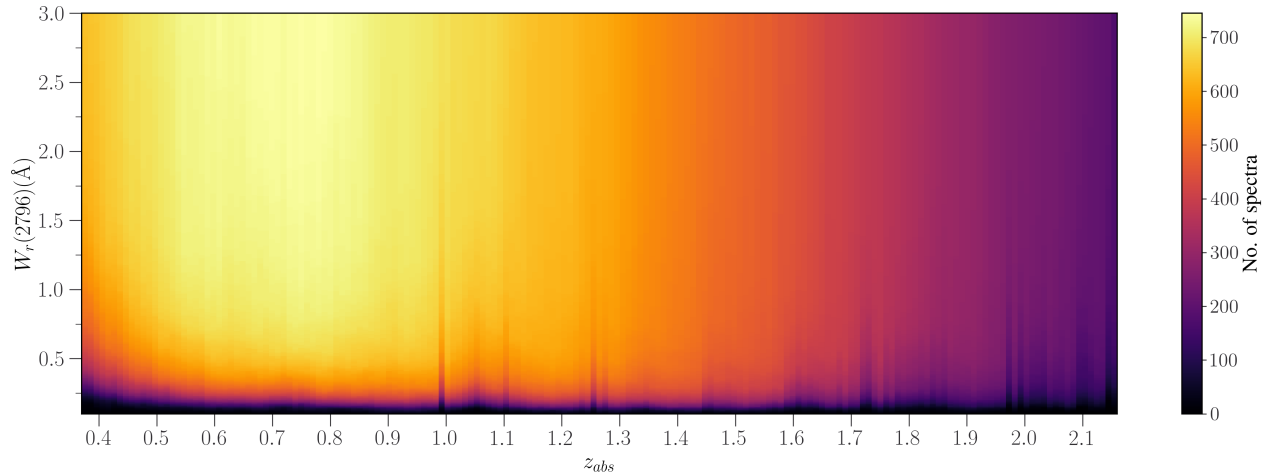


Figure 7. Redshift path sensitivity function $g(z, W_{min})$ for the Mg II 2796 Å at the 3σ significance level i.e. $N_\sigma = 5$. The plot shows the number of quasar spectra in which a Mg II absorption line of rest frame equivalent width W_r could have been detected, as a function of redshift. The dark vertical bands signify bright night-sky lines or atmospheric absorption. The depression at $z \approx 1.05$ corresponds to the wavelength where the dichroic splits the two arms of the spectrograph.

dichroic. This leads to a discontinuity in the spectra that is reflected in the plot at 5700 Å at $z \simeq 1.0$ (Childress et al. 2017). The dark vertical lines in the figure show atmospheric absorption bands.

Using our definition of $g(W, z)$, we can define the comoving path ΔX . The comoving path ΔX is a measure of the distance that the light from a quasar has traveled to reach the observer. This is an important quantity in the context of an absorption line survey, because it represents the length of the path that the survey covers in redshift space. For example, a survey with a large comoving path length covers a larger volume of the Universe and is therefore more sensitive to rare or distant absorbers. ΔX can be thought of as a measure of the survey depth or volume. Over a finite redshift interval from z_1 to z_2 , this is expressed analytically as

$$\Delta X(W_r) = \int_{z_1}^{z_2} g(W_r, z) \frac{dX}{dz} dz, \quad (22)$$

where, assuming a flat Universe,

$$\frac{dX}{dz} = \frac{(1+z)^2}{\Omega_M(1+z)^3 + \Omega_\Lambda}. \quad (23)$$

This term represents the comoving distance per unit redshift, which is a fundamental quantity that characterizes the expansion history of the Universe.

4. RESULTS

The main results we present are the Mg II $\lambda 2796$ rest-frame equivalent width distribution and the redshift path density of Mg II doublets. These comprise the two most extensively studied distributions measured for Mg II absorption systems in the northern hemisphere using low resolution quasar spectroscopy (e.g., Steidel & Sargent 1992; Nestor et al. 2005; Seyffert et al. 2013; Zhu & Ménard 2013). Thus, they provide robust data by which to compare our first view of Mg II absorber characteristics in the southern hemisphere.

In Section 5, we introduce a method for estimating the cosmic mass density of Mg⁺ ions using low-resolution surveys as informed by high-resolutions survey line measurements.

4.1. Equivalent Width Distribution

The equivalent width distribution is defined as the probability density function $f(W_r) = d^2N/dW_r dX$. This gives the relative number of absorption systems with rest-frame equivalent width W_r in redshift range z per unit equivalent width per unit comoving redshift path.

In practice, the equivalent width distribution is computed in discrete bins. For a given equivalent width bin ΔW_r centered at W_r over a given comoving redshift path $\Delta X(W_r)$, as defined in Eq. 22, we have

$$f(W_r) = \frac{N}{\Delta W_r \Delta X(W_r)}, \quad (24)$$

where N is the number of absorbers in the equivalent bin. In Figure 8, we show the equivalent width distribution of Mg II $\lambda 2796$ Å absorbers in our sample. The points are the mean W_r in the bins and the horizontal error bars are the equivalent width bin sizes. The vertical error bars are based on Poisson statistics.

For surveys sensitive to $W_r < 0.05$ Å, a Schechter function (Schechter 1976) provides a good description of the distribution function (Kacprzak & Churchill 2011; Mathes et al. 2017). However, since we used low resolution spectra for this work, we are 50% complete at $W_r \simeq 0.3$ Å. For such completeness levels, the distribution is dominated by the exponential term (e.g., Steidel & Sargent 1992; Nestor et al. 2005; Cooksey et al. 2013; Seyffert et al. 2013; Zhu & Ménard 2013). We thus adopt

$$f(W_r) = \frac{N_*}{W_*} \exp\left(-\frac{W}{W_*}\right). \quad (25)$$

Table 2. Equivalent Width Fitted Parameters

Reference	W_* (Å)	N_*
Steidel & Sargent (1992) [†]	0.66 ± 0.11	1.55 ± 0.20
Nestor et al. (2005) [†]	0.702 ± 0.017	1.187 ± 0.052
Seyffert et al. (2013)	0.714 ± 0.005	0.506 ± 0.015
OzDES (this work)	0.76 ± 0.04	0.44 ± 0.08

[†]Normalization is dN/dz . N_* not comparable to OzDES.

Using the LMFIT python package (Newville et al. 2014), we obtained best-fitted parameters of $N_* = 0.44 \pm 0.08$ and $W_* = 0.76 \pm 0.04$ Å. We performed the fit on the binned data. The bins have equal widths in dex.

In Figure 8, the solid blue line represents the best-fit exponential function. The shape of the equivalent width distribution function aligns with findings from earlier low-resolution surveys (e.g., Steidel & Sargent 1992; Nestor et al. 2005; Seyffert et al. 2013; Zhu & Ménard 2013). A comparison of our $f(W_r)$ fit parameters N_* and W_* to those from Steidel & Sargent (1992), Nestor et al. (2005), and Seyffert et al. (2013) is presented in Table 2. It is essential to note that neither Steidel & Sargent (1992) nor Nestor et al. (2005) normalize their equivalent width distribution by the comoving redshift path $\Delta X(W_r)$. Consequently, our normalization N_* is directly comparable only with Seyffert et al. (2013), who fitted exponential function using the $f(W_r) = k \exp(\alpha W_r)$. To equate Eq. 25, we converted k and α from Seyffert et al. (2013) to N_* and W_* using the relations: $W_* = -1/\alpha$ and $N_* = kW_*$.

Comparing W_* values obtained by Steidel & Sargent (1992), Nestor et al. (2005), and Seyffert et al. (2013), we find that the OzDES value is statistically in agreement, if not trending a slightly higher. As shown by Chen et al. (2017, see their Figure 9), the value of W_* is known to evolve over the redshift range of the OzDES sample, $0.3 \leq z \leq 2.2$. The value decreases from $W_* \simeq 0.9$ Å at $z \simeq 2.2$ to $W_* \simeq 0.6$ Å at $z \simeq 0.3$. All W_* values listed in Table 2 are determined over virtually identical redshift ranges for which the median redshifts of the samples are $\langle z \rangle \sim 1.1$. The median redshift of the OzDES science sample is $\langle z \rangle = 1.14$. We note that the OzDES measurement of $W_* = 0.76$ is fully consistent with the maximum likelihood value of $W_* = 0.74$ Å found by Chen et al. (2017, see their Table 5) for this redshift based on a meta-study of MgII surveys covering $0.37 \leq z \leq 7.1$. Comparing the OzDES N_* value with Seyffert et al. (2013), OzDES is statistically consistent. If we renormalize the OzDES N_* to yield the equivalent width per unit redshift, i.e., $f(W_r) \cdot \{\Delta X(W_r)/\Delta Z(W_r)\}$, we can compare the N_* values of Steidel & Sargent (1992) and Nestor et al. (2005).

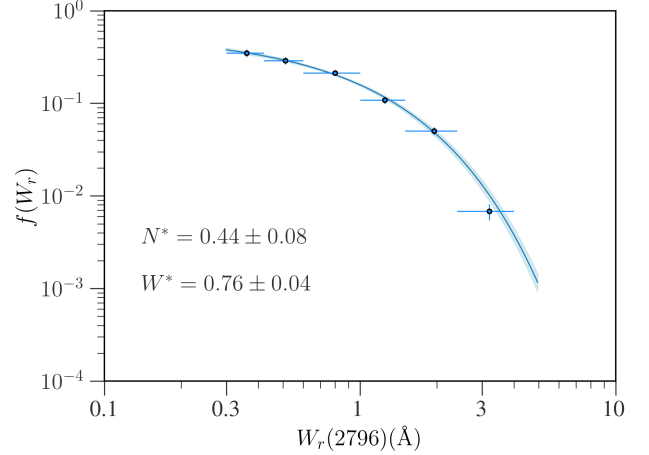


Figure 8. The rest-frame equivalent width distribution function, $f(W_r) = d^2W_r/dW_r dX$, of the MgII $\lambda 2796$ transition for the OzDES science sample. The vertical error bars are the Poisson uncertainty. The horizontal bars are the equivalent width bin sizes. The solid blue curve is the fit for the exponential function (Eq. 25). Comparison of the fitted parameters W_* and N_* with other surveys are listed in Table 2.

For OzDES, $\Delta Z(0.3) = 690$, and $\Delta X(0.3) = 1614$, giving $\Delta Z(0.3)/\Delta X(0.3) = 2.34$, which yields $N_* = 1.02 \pm 0.19$ for OzDES. This value is consistent with that of Nestor et al. (2005, $N_* = 1.19 \pm 0.05$), but smaller than that value measured by Steidel & Sargent (1992).

4.2. Absorber Path Density

The redshift path density, dN/dz , quantifies the number of absorbers per unit redshift for absorbers above a given W_r threshold. For a survey in which the W_r threshold is variable with redshift, dN/dz is defined as (e.g., Lanzetta et al. 1987),

$$\frac{dN}{dz} = \sum_i \frac{1}{\Delta Z(W_i)} \quad (26)$$

$$\sigma_{dN/dz} = \sum_i \frac{1}{\Delta Z^2(W_i)},$$

where $\Delta Z(W_i)$ is the total redshift path covered in the survey for absorber i having rest-frame equivalent width W_i . $\sigma_{dN/dz}$ is the uncertainty in dN/dz . The sum is taken over all absorbers in the redshift interval for which dN/dz is being measured. If the redshift interval spans from z_1 to z_2 , then the redshift path for a system with $W_r = W_i$ in this interval is given by

$$\Delta Z(W_r) = \int_{z_1}^{z_2} g(W_r, z) dz. \quad (27)$$

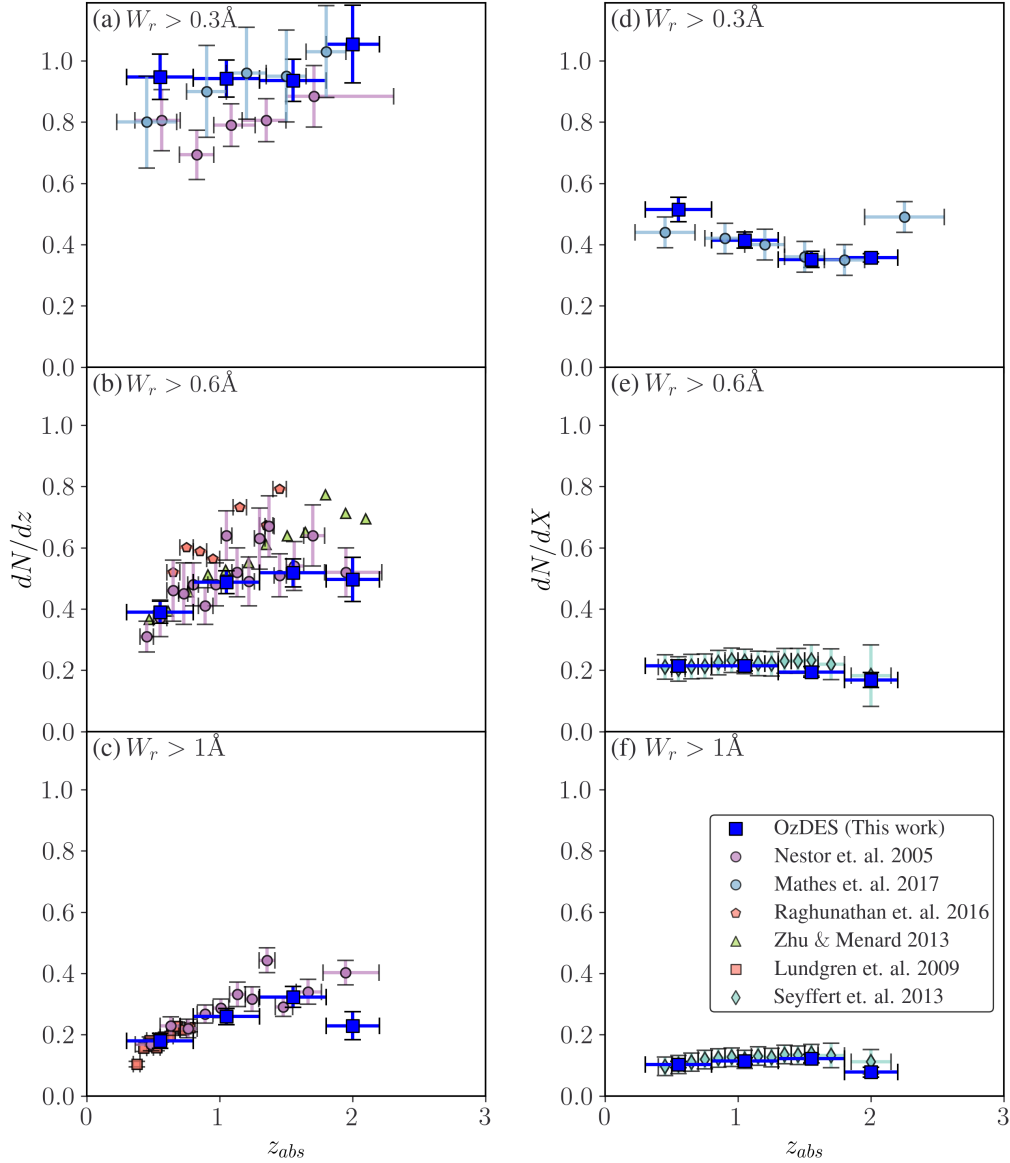


Figure 9. (left panels) The redshift path density $d\mathcal{N}/dz$ of Mg II absorber samples with lower threshold of (a) $W_r \geq 0.3 \text{ \AA}$, (b) $W_r \geq 0.6 \text{ \AA}$, and (c) $W_r \geq 1 \text{ \AA}$. (right panels) The comoving path density $d\mathcal{N}/dX$ for (d) $W_r \geq 0.3 \text{ \AA}$, (e) $W_r \geq 0.6 \text{ \AA}$, and (f) $W_r \geq 1 \text{ \AA}$. The OzDES systems are the blue data to which we compare the available northern hemisphere works of Steidel & Sargent (1992), Nestor et al. (2005), Seyffert et al. (2013), Zhu & Ménard (2013), Raghunathan et al. (2016), and Mathes et al. (2017). Note, that in panel (b) Raghunathan et al. (2016) compute $d\mathcal{N}/dz$ for $W_r > 0.65 \text{ \AA}$.

Similarly, $d\mathcal{N}/dX$, the number of absorbers per unit comoving path length, is defined as

$$\begin{aligned} \frac{d\mathcal{N}}{dX} &= \sum_i \frac{1}{\Delta X(W_i)} \\ \sigma_{d\mathcal{N}/dX} &= \sum_i \frac{1}{\Delta X^2(W_i)}, \end{aligned} \quad (28)$$

where $\Delta X(W_i)$ is given by Eq. 22 for absorber i having rest-frame equivalent width W_i .

In Figure 9, we show $d\mathcal{N}/dz$ and $d\mathcal{N}/dX$ as a function of redshift for Mg II absorbers in the OzDES survey (blue

data points). These data are listed in Table 3. We examine the path densities in four redshift bins such that they each roughly have 150 absorbers. We adopted and show subsamples having lower thresholds of $W_r \geq 0.3 \text{ \AA}$, $W_r \geq 0.6 \text{ \AA}$, and $W_r \geq 1 \text{ \AA}$ in order to directly compare our southern hemisphere measurements with the northern hemisphere data of Steidel & Sargent (1992), Nestor et al. (2005), Lundgren et al. (2009), Seyffert et al. (2013), Zhu & Ménard (2013), and Raghunathan et al. (2016). For all subsamples, we find that the southern hemisphere path densities are consistent with the northern hemisphere path densities over the similar redshift ranges.

Table 3. $d\mathcal{N}/dz$, $d\mathcal{N}/dX$ and $\Omega_{\text{MgII}} \times 10^{-6}$

Redshift	$(W_r \geq 0.3 \text{ \AA})$		$(W_r \geq 0.6 \text{ \AA})$		$(W_r \geq 1.0 \text{ \AA})$		(Sum)	(Integral)
	$d\mathcal{N}/dz$	$d\mathcal{N}/dX$	$d\mathcal{N}/dz$	$d\mathcal{N}/dX$	$d\mathcal{N}/dz$	$d\mathcal{N}/dX$	$\Omega_{\text{MgII}}(z)$	$\Omega_{\text{MgII}}(z)$
(0.33,0.80]	0.95 ± 0.07	0.51 ± 0.04	0.39 ± 0.04	0.21 ± 0.02	0.18 ± 0.02	0.10 ± 0.01	$0.47^{+0.26}_{-0.11}$	$0.76^{+0.28}_{-0.16}$
(0.80,1.30]	0.94 ± 0.06	0.41 ± 0.03	0.49 ± 0.04	0.21 ± 0.02	0.26 ± 0.03	0.11 ± 0.01	$0.42^{+0.18}_{-0.08}$	$0.69^{+0.18}_{-0.13}$
(1.30,1.80]	0.93 ± 0.06	0.35 ± 0.03	0.52 ± 0.04	0.19 ± 0.02	0.32 ± 0.03	0.12 ± 0.01	$0.41^{+0.16}_{-0.08}$	$0.65^{+0.19}_{-0.14}$
(1.80,2.20)	1.05 ± 0.12	0.36 ± 0.01	0.50 ± 0.07	0.17 ± 0.02	0.23 ± 0.04	0.08 ± 0.02	$0.24^{+0.26}_{-0.08}$	$0.47^{+0.32}_{-0.11}$

Not all northern surveys published results for all three equivalent width thresholds. Compared to Nestor et al. (2005), the OzDES $d\mathcal{N}/dz$ values for the $W_r \geq 0.3 \text{ \AA}$ sample are slightly higher, but appear to be in excellent agreement with Steidel & Sargent (1992). For $W_r \geq 0.6 \text{ \AA}$, the OzDES $d\mathcal{N}/dz$ values are consistent with the three surveys of Nestor et al. (2005), Zhu & Ménard (2013), Raghunathan et al. (2016), though they appear to cluster toward the lower values within the “cloud” formed by these data. For $W_r \geq 1.0 \text{ \AA}$, the OzDES $d\mathcal{N}/dz$ values are consistent with the surveys of Nestor et al. (2005) and Lundgren et al. (2009). In terms of $d\mathcal{N}/dX$, the OzDES values are in full agreement with the published values of Seyffert et al. (2013) for $W_r \geq 0.6 \text{ \AA}$ and $W_r \geq 1 \text{ \AA}$. Though we do not show the comparison on Figure 9, the OzDES $d\mathcal{N}/dX$ for the $W_r \geq 0.3 \text{ \AA}$ sample is consistent with the values from the high-resolution survey of Mathes et al. (2017).

5. THE MASS DENSITY

The mass density, $\Omega = \rho/\rho_c$, of an elemental species or ion is defined as the ratio of its cosmic mass density to the critical density of the universe, $\rho_c = 3H^2/8\pi G$. In general form, we can define the MgII mass density as

$$\Omega_{\text{MgII}}(z) = \frac{H_0}{c} \frac{m_{\text{Mg}}}{\rho_c} \langle N \rangle \frac{d\mathcal{N}}{dX} \quad (29)$$

where $\langle N \rangle$ is the measured mean column density of the population of MgII absorbers, and $d\mathcal{N}/dX$ is their comoving path density. We have

$$C = \frac{H_0}{c} \frac{m_{\text{Mg}}}{\rho_c} = 3.214 \times 10^{-22} \text{ cm}^2, \quad (30)$$

where $m_{\text{Mg}} = 4.036 \times 10^{-23} \text{ g}$ is the mass of a magnesium atom and $\rho_c = 9.77 \times 10^{-30} \text{ g cm}^{-3}$ is the present-day critical density of the universe.

The product $\langle N \rangle d\mathcal{N}/dX$ yields the total column density of the population per unit of comoving path length and can be written

$$\langle N \rangle \frac{d\mathcal{N}}{dX} = \frac{N_{\text{tot}}}{\Delta X} = \frac{1}{\Delta X} \sum_i N_i, \quad (31)$$

where the sum is taken over all absorbers in the sample over the finite redshift range for the calculation. Alternatively, if

the column density distribution function, $f(N)$, is measured, we can write $\langle N \rangle d\mathcal{N}/dX$ in integral form as the first moment of the column density distribution function,

$$\langle N \rangle \frac{d\mathcal{N}}{dX} = \langle N \rangle \int_{N_L}^{N_U} f(N) dN = \int_{N_L}^{N_U} f(N) N dN, \quad (32)$$

where N_L and N_U are the minimum and maximum observed column density of the sample, and the column density distribution function has been normalized to $d\mathcal{N}/dX$.

Clearly, accurate estimation of the column densities of MgII absorbers is crucial in determining the value of Ω_{MgII} . One of the most reliable methods for estimating column densities is to fit resolved absorption profiles with a Voigt profiles. Voigt profile fitting is appropriate only for high-resolution absorption line spectra where the atomic plus Gaussian line broadening can be resolved. However, for our study, we only have low-resolution spectra available, and as a result, we must resort to alternative methods for estimating the column densities of the MgII absorbers in our survey.

Unfortunately, the relatively straight forward apparent optical depth method (AOD, e.g., Savage & Sembach 1991) is also not accurate for low resolutions spectra, as unresolved saturation can yield underestimates as large as ~ 1 dex in the column densities (also see Jenkins 1996). Likewise, curve of growth (COG) methods also have their limitations. The equivalent widths of MgII absorption lines reflect their multi-component nature in that they scale with the number of components, each of which has a unique column density (e.g., Petitjean & Bergeron 1990; Churchill et al. 2003; Churchill et al. 2020). A such, a unique COG relation cannot be applied to multi-component absorption lines.

5.1. Monte Carlo Modeling

We have developed a Monte Carlo method for estimating the total column density (N_{tot} , Eq. 31) and the mean column density ($\langle N \rangle$, Eq. 32) for a survey of low-resolution absorption lines. The model is informed by the relationship between equivalent width and system-total column density from a database of high-resolution MgII absorption profiles for which Voigt profile analysis has been performed.

In summary, our approach to calculating Ω_{MgII} is that we use a Monte Carlo method to obtain an estimated column density for each and every MgII system in the OzDES survey. This

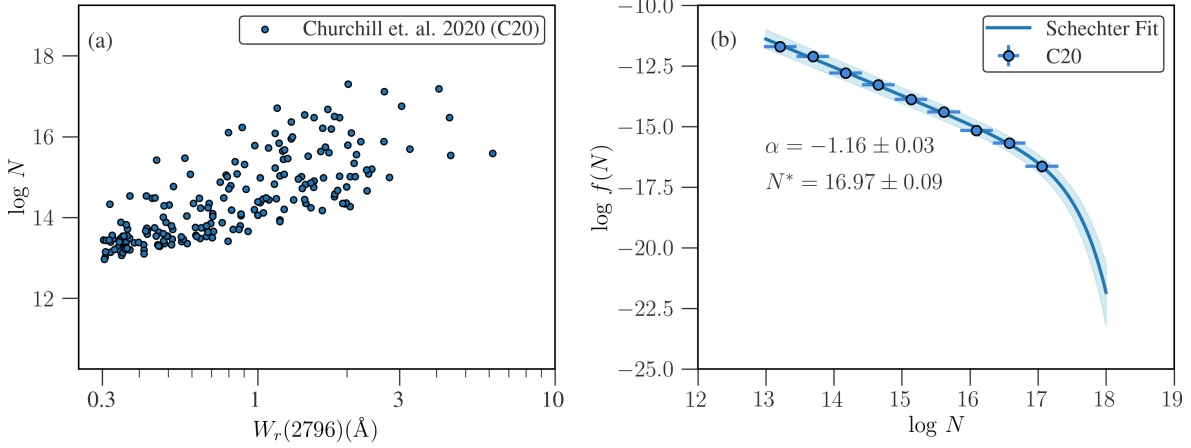


Figure 10. (a) The system-total column densities of MgII absorbers obtained from Voigt profile fitting of high-resolution spectra from C20 versus rest-frame equivalent width. Only absorbers with $W_r > 0.3 \text{ \AA}$ are included to ensure comparability with the OzDES science sample. (b) The column density distribution function of the C20 sample. The distribution is well fitted by a Schechter function (see Eq. 33) with $\alpha = -1.16 \pm 0.03$ and $\log(N_*/\text{cm}^{-2}) = 16.97 \pm 0.09$.

provides a single “realization” of the column densities for the entire observed sample of absorbers. We then compute $\Omega_{\text{MgII}}(z)$ from Eq. 29 using both the summation (Eq. 31) and integral (Eq. 32) formalism. In this way, each Monte Carlo realization provides two estimates of the mass density. We then implement 10^5 Monte Carlo realizations of the OzDES sample from which we determine a mean mass density and its uncertainty.

In Figure 10(a), we show the N - W_r pairs from the sample of Churchill et al. (2020, hereafter C20). We use this sample to inform our Monte Carlo model. We limited our study to systems with $W_r \geq 0.3 \text{ \AA}$, as this equivalent width is representative of the minimum value in the OzDES science sample. We also limited our study to absorbers residing in the redshift range for detecting MgII doublets in the OzDES spectra. A total of 198 systems met these selection criteria. In Figure 10(b), we show the column density distribution function, which is well fitted by a Schechter function,

$$f(N)dN = \Phi_0 \left(\frac{N}{N_*} \right)^\alpha \exp \left\{ -\frac{N}{N_*} \right\} \frac{dN}{N_*} \quad (33)$$

where α is the power-law slope, N_* is the characteristic column density, and Φ_0 is the normalization. Using LMFIT (Newville et al. 2014), we obtained least-square fitted parameters $\alpha = -1.16 \pm 0.03$ and $\log(N_*/\text{cm}^{-2}) = 16.97 \pm 0.09$.

Although the full C20 sample can be convincingly fitted with a single Schechter function over the range $W_r \in (0.3, 6.168) \text{ \AA}$, examination of Figure 10(a) shows a clear trend between N and W_r , indicating that the column density distribution function varies with equivalent width. Note that there is a clear lower boundary to N that increases with increasing W_r . In addition, for the smallest absorbers ($W_r \sim 0.3 \text{ \AA}$) the range of N is on the order of 1 dex, where as the range is ~ 2 dex for stronger absorbers ($W_r \sim 1.0 \text{ \AA}$).

In Appendix A, we detail how we treat the W_r dependence of the column density distribution function and de-

scribe how the Monte Carlo model estimates the column density associated with a MgII system of a given equivalent width. We also describe how we compute N_{tot} and $\langle N \rangle$ for a given Monte Carlo realization of the OzDES survey. In Appendix B, we quantify the degree to which the model is consistent with the column density distribution measured from the high-resolution MgII sample. In Appendix C, we explain how we estimate Ω_{MgII} and its uncertainty from 10^5 Monte Carlo realizations of the OzDES science sample.

5.2. OzDES Mass Density

In Table 3, we present Ω_{MgII} for the science sample. We include both the summation method (Eq. 31) and the integral method (Eq. 32). We computed Ω_{MgII} in four redshift bins for $W_r \geq 0.3 \text{ \AA}$. We illustrate Ω_{MgII} in Figure 11 (also see Figure 15 in Appendix C). The red points represent the summation method and the purple points represent the integral method. In each redshift bin, we ran 10^5 Monte Carlo realizations of the OzDES sample. The quoted best-values and their uncertainties are determined as described in Appendix C. Within the 1σ uncertainties, the summation and integral methods are consistent with one another.

Over the redshift range $0.3 \leq z \leq 2.2$, there seems to be little-to-no evidence for evolution in the cosmic mass density of Mg⁺ ion, though the mass density weakly trends toward higher values over the ~ 7 Gyr cosmic time corresponding to the studied redshift range. The integral values are marginally higher than the summation values because the integral method includes additional area under the column density distribution function at large column densities (we integrate to $N_i = \infty$). This results in a slightly larger mean column density, $\langle N \rangle$, for the sample, as compared to the summation method, which terminates at the maximum column density of a realization.

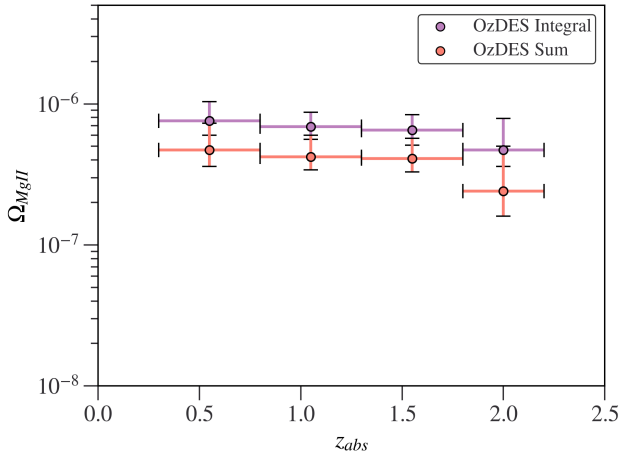


Figure 11. The mass density, Ω_{MgII} , for the the OzDES science sample ($W_r \geq 0.3 \text{ \AA}$). Values have been computed using both the summation formalism (Eq. 31, red points) and as an integration method (Eq. 32, purple points).

6. DISCUSSION

The analysis of intervening absorption lines is but one of many approaches to studying cosmological evolution. Measuring evolution in the global star formation density provides insights into the average rate at which baryonic mass converts into stars across cosmic time (e.g., Reddy & Steidel 2009; Oesch et al. 2013, 2014; Madau & Dickinson 2014; Bouwens et al. 2015). Similarly, measuring evolution in the global energy density of ultraviolet radiation provides insights into the ionization history of the universe (e.g. Schiminovich et al. 2005; Reddy & Steidel 2009; Oesch et al. 2013, 2014; Bouwens et al. 2015). Complimentary to such measurements is the global mass density of gas, which provides insights into the cosmic evolution of the gas mass partaking in the baryon cycle of galaxies (e.g., Shull et al. 2012; Nicastro et al. 2018; Driver 2021). In particular, comparing evolution between the mass densities of various ions provides insights into both the chemical evolution of various chemical species and their relative ionization conditions.

Whereas the mass densities of HI absorbers (e.g., Songaila & Cowie 2010; Crighton et al. 2015; Rao et al. 2017; Ho et al. 2021), of CIV absorbers (e.g., Songaila 2001, 2005; Schaye et al. 2003; Danforth & Shull 2008; Becker et al. 2009; Ryan-Weber et al. 2009; Cooksey et al. 2010; D’Odorico et al. 2010, 2013; Simcoe et al. 2011; Boksenberg & Sargent 2015; Díaz et al. 2016; Bosman et al. 2017; Codoreanu et al. 2018; Manuwal et al. 2021; Davies et al. 2023b), and of SiIV absorbers (e.g., Shull et al. 2014; Cooksey et al. 2011; Songaila 2001; Scannapieco et al. 2006; Boksenberg & Sargent 2015; Codoreanu et al. 2018; D’Odorico et al. 2022) have been well documented, there are only three previous works that present measurements of Ω_{MgII} . The first is Mathes et al. (2017, hereafter M17), who employed AOD column densities of 1180 MgII absorbers with $0.003 \leq W_r \leq 8.5 \text{ \AA}$ covering $0.14 \leq z \leq 2.64$ measured in 602 HIRES and

UVES quasar spectra. The second is Codoreanu et al. (2017, hereafter C17), who used Voigt profile column densities of 52 MgII absorbers with $0.12 \leq W_r \leq 3.67 \text{ \AA}$ covering $2.0 \leq z \leq 5.4$ measured in four X-Shooter quasar spectra. The third is Sebastian et al. (2023, hereafter S23), who also used Voigt profile column densities of X-Shooter quasar spectra. The S23 measurements were based on 280 MgII absorbers in the redshift range $2.0 \leq z \leq 6.4$ identified in 42 spectra from the E-XQR-30 survey of (D’Odorico et al. 2023) as analyzed by Davies et al. (2023a).

As described in Section 5, we have developed a Monte Carlo method to estimate the mass density of MgII absorbers, Ω_{MgII} , from equivalent widths measured in low-resolution spectra as informed by high-resolution spectra. We have applied this method to the OzDES sample of MgII absorbers over the redshift range $0.3 \leq z \leq 2.2$. It is of interest to compare the OzDES MgII mass density to the works M17 and to examine evolution through comparison with the $2 \leq z \leq 6.5$ measurements by C17 and S23.

6.1. The Mass Density at $0.3 \leq z \leq 2.2$

As seen in Figure 11, the OzDES Ω_{MgII} measurements indicate little-to-no evolution for $z \leq 2$. This lack of strong evolution following Cosmic Noon is astrophysically plausible. Though dN/dX of the strongest absorbers ($W_r > 1.0 \text{ \AA}$) decreases from Cosmic Noon to $z \sim 0.3$, it is no more than a $\sim 30\%$ decline during this cosmic period (Seyffert et al. 2013). We note that the corresponding dN/dX measured with OzDES is highly consistent with this very mild evolution (see Figure 9(f)). Moreover, in this redshift regime (1) the ultraviolet background is declining by a two orders of magnitude (Haardt & Madau 2012; Khaire & Srianand 2019; Faucher-Giguère 2020), so that absorbing gas structures are evolving toward lower ionization conditions, and (2) the metallicity of MgII absorbing structures (sub-Lyman limit systems and sub-damped Ly α absorber) are increasing by up to an order of magnitude (e.g., Fumagalli et al. 2016; Lehner et al. 2022). Taken together, these statistical astronomical phenomena could yield an overall outcome of a more-or-less constant mass density over the redshift range $0.3 \leq z \leq 2.2$.

In Figure 12(a), we present a comparison between the OzDES Ω_{MgII} values and those reported by M17 (orange points). The maximum equivalent width in the OzDES survey is $W_r = 3.5 \text{ \AA}$, where as 7/1180 of the systems in the M17 survey have $W_r > 4 \text{ \AA}$. Both works cover the approximate redshift range $0.3 \leq z \leq 2.2$ in four similar redshift bins. We present the OzDES values computed for both the summation (Eq. 31, purple points) and integral (Eq. 32, red points) methods. As the values of M17 are based on AOD column densities, and the AOD method provides only lower limits in the case of unresolved saturation (e.g., Savage & Sembach 1991; Jenkins 1996), the M17 Ω_{MgII} values should be viewed as lower limits.

As seen in Figure 12(a), the OzDES Ω_{MgII} values reside roughly a factor of ten (1 dex) above the Ω_{MgII} lower limits of M17. Again, one clear reason for the substantially larger

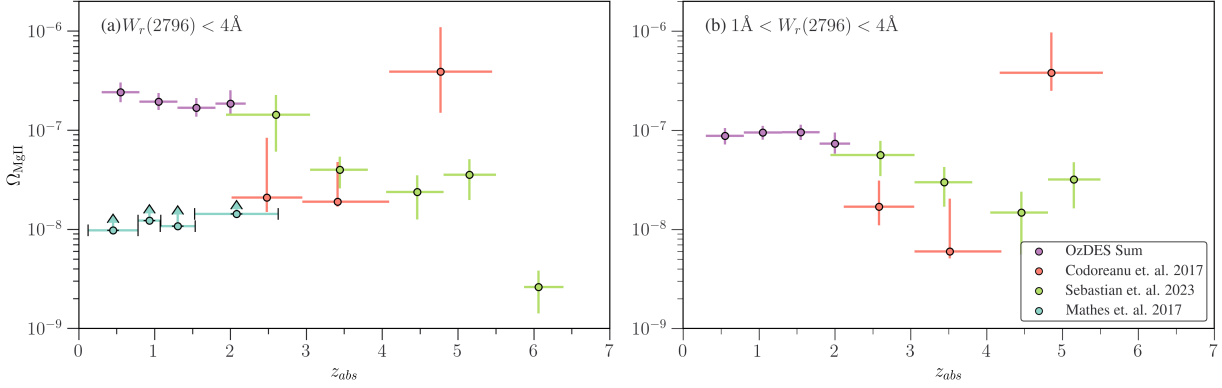


Figure 12. Comparison of redshift evolution of Ω_{MgII} between the OzDES, **M17**, **C17**, and **S23** surveys. The upper limit on the column density in the **M17** survey was $\log(N_{\text{MgII}}/\text{cm}^{-2}) \simeq 15$. (a) Absorbers with $W_r < 4 \text{ \AA}$. The purple OzDES points are based on the summation method. The green points ($z \geq 2$) are from **C17**. The blue points are the upper limits from **M17** (note, however, that 7/1180 of their systems have $W_r > 4 \text{ \AA}$). The orange points are from **S23**. (b) Absorbers limited to the range $1 \leq W_r < 4 \text{ \AA}$. Data points are the same as in panel (a).

OzDES values is that fact the AOD method provides only lower limits for Ω_{MgII} because of it provides lower limits on the MgII column densities when the absorption profiles suffer unresolved saturation. The largest AOD column density lower limits in the **M17** sample are $\log(N_{\text{MgII}}/\text{cm}^{-2}) \simeq 15.0$. Visual inspection of Figure 10 reveals that roughly 30% of the absorbers in the **C20** sample have $\log(N_{\text{MgII}}/\text{cm}^{-2}) > 15.0$ for almost the complete range of MgII rest-frame equivalent widths. Though the largest system-total column densities are $\log(N_{\text{MgII}}/\text{cm}^{-2}) \simeq 16.5$ from the Voigt profile fits of **C20**, the Monte Carlo method draws from a Schechter distribution function, which can yield even larger column densities for $W_r > 3 \text{ \AA}$ (though with a vanishing frequency). Thus, considering Eq. 29, which shows that the calculation of Ω_{MgII} is proportional to the mean column density of the population, it is clear that the Monte Carlo method we applied to the OzDES MgII systems would yield values that are substantially larger than the lower limits of **M17**.

A similar outcome has been found for Ω_{CIV} , as demonstrated by **Cooksey et al. (2013)**. They used the SDSS DR7 quasar catalog (**Schneider et al. 2010**) and found $\sim 15,000$ CIV absorbers in $\sim 26,000$ quasar sight lines. They computed Ω_{CIV} using AOD column densities, even though they were fully aware that the low-resolution SDSS spectra would yield a lower limit on Ω_{CIV} in each redshift bin. In comparing their value to several high-resolution works that used Voigt profile column densities, they found that their AOD-based estimates of Ω_{CIV} were systematically below those of the high-resolution works.

6.2. The Mass Density at $0.3 \leq z \leq 6.4$

Together, the OzDES, **C17**, and **S23** surveys span Cosmic Noon and the epoch of HeII reionization and probe the very end of the epoch of HI reionization.

C17 conducted a survey of four quasars and found 52 intervening MgII absorbers in the range $2 \leq z \leq 5.4$. The column densities of the MgII absorbers were estimated using Voigt profile fitting. They computed Ω_{MgII} in three redshift bins for two sample using the summation method (see

Eq. 31). The first sample was for systems with $W_r \leq 4 \text{ \AA}$, and the second was for systems with $1.0 \leq W_r \leq 4 \text{ \AA}$. The maximum system-total column density (i.e., sum of components) in their sample was $\log(N/\text{cm}^{-2}) = 16.4$. To ensure a self-consistent comparison between OzDES and **C17**, we recomputed the OzDES Ω_{MgII} using the equivalent width and column density ranges of **C17**. **S23** adopted survey results of **Davies et al. (2023a)**, which yielded 280 intervening MgII absorbers in the range $1.9 \leq z \leq 6.4$ from 42 quasar spectra. The column densities of the MgII absorbers were estimated using Voigt profile fitting. Using these data, **S23** computed Ω_{MgII} in five redshift bins using the summation method (see Eq. 31) including all absorbers in their sample.

In Figure 12(a), we present Ω_{MgII} for MgII absorbers with $W_r < 4 \text{ \AA}$ and, in Figure 12(b), we present MgII absorbers with $1 \leq W_r < 4 \text{ \AA}$. We present the OzDES values computed for both the summation (Eq. 31) and integral (Eq. 32) methods. Both the **C17** and **S23** were computed using the summation method. For the $W_r < 4 \text{ \AA}$ sample, we also include the upper limits computed by **M17**, but we note that 7/1180 (0.6%) of their systems have $W_r > 4 \text{ \AA}$.

As seen in Figure 12(a,b), the **C17** values indicate a ~ 1 dex decline from $z \sim 5$ to $z \sim 3.5$ and are consistent with no evolution from between $z \sim 4$ to $z \sim 2$. This would suggest a 10-fold decrease in the mass density of the the Mg^+ ion as traced by MgII absorbers over a timescale of $\simeq 0.6$ Gyr (the approximate main sequence lifetime of a B8 or B9 star!)². Taken at face value, the OzDES results would then imply a rapid increase of ~ 1 dex around $z \sim 2$. The OzDES results would constitute a second dramatic evolution over a period of ~ 1 Gyr that would be followed by no evolution from $z \sim 2$ down to $z \sim 0.3$ (roughly 7 Gyr).

²The **C17** sample is based on only four quasar spectra. The reason we believe that there is the factor of 10 difference is due to cosmic variance over this small sample. The maximum column densities in the $z < 4.5$ bins is $\log(N/\text{cm}^{-2}) = 15.3$, whereas the maximum in the $z > 4.5$ bin is 16.4. This neatly explains the factor of ~ 10 difference.

A different evolutionary picture emerges when we compared the OzDES mass densities to those measured by S23. As seen in Figure 12(a,b), together these surveys would suggest a relatively smooth factor of 10 increase from $z \sim 5$ to Cosmic Noon followed by a plateau from $z \sim 2$ to $z \sim 0.4$ (we note that the highest redshift point of S23 is the least secure and that no $W_r > 1 \text{ \AA}$ absorbers were detected in this redshift bin). This smoother evolution would be a more astrophysically plausible evolution in that, as pointed out by S23, it is consistent with the factor-of-several increase in dN/dX of the strongest Mg II absorbers from $z \sim 6$ to Cosmic Noon (Matejek et al. 2013; Chen et al. 2017; Sebastian et al. 2023).

6.3. How Might the Mass Density Evolve?

There are multiple ways in which Ω_{MgII} could evolve: (1) metallicity evolution, (2) ionization evolution, (3) structure evolution, (4) all of the above. These astrophysical changes would manifest as evolution in the comoving redshift path density, which is the normalization to the column density distribution function. Alternatively, they could manifest as evolution in the shape of the column density distribution function. Or, both the normalization and the shape could evolve.

If the evolution is manifest in the normalization, $dN/dX = (H_0/c)n_0\sigma_0$, then it would imply a change in either the comoving spatial number density, n_0 , and/or the cross section of the absorbing structure, σ_0 . Either could indicate chemical, ionization and/or structure evolution of the absorber. If the evolution is manifest in the shape of the column density distribution function, then it would imply changes in the conditions that create, sustain, and destroy smaller sized absorbers relative to larger sized absorbers (or vice versa). Evidence of shape evolution may even suggest that the types of astrophysical environments or overdensities populated by the Mg II absorbers evolve.

Evolution in the column density distribution function, whether due to evolution in its normalization, dN/dX , and/or its functional shape, such as its power-law index α , cannot directly inform us of the underlying astrophysics in the evolution of Mg II absorbing structures. At a minimum, deeper insights requires ionization modeling, which requires observations of multiple ions. However, there are direct functional relationships between Ω_{MgII} , dN/dX , and the column density distribution function such that their measurements should yield a self-consistent picture of Mg II absorbers. In particular, such relationships have been exploited to measure the evolution in the equivalent width distribution function from $z = 7$ to $z = 0$ (Churchill et al. 2024).

If the lack of evidence for evolution in the OzDES Ω_{MgII} values for redshift following Cosmic Noon are taken at face value, we might infer that the various cosmic conditions governing the global mass density of Mg II absorbers have reached a steady state balance following the epoch of peak activity in the low-ionization gaseous component of the universe.

6.4. Comparison to Ω_{HI} and Ω_{dust}

A comparison of $\Omega_{\text{MgII}}(z)$ and $\Omega_{\text{HI}}(z)$ can provide some insights into the redshift evolution of the ratio of the mean column densities of the population of Mg II-selected absorbers relative to that of the population of HI-selected damped Ly α absorbers (DLAs), which are defined to have $\log(N_{\text{HI}}/\text{cm}^{-2}) \geq 20.3$ (Wolfe et al. 1986). From Eq. 29, we write

$$\frac{\langle N_{\text{MgII}} \rangle}{\langle N_{\text{HI}} \rangle} = \frac{m_{\text{H}}}{m_{\text{Mg}}} \frac{(dN/dX)_{\text{HI}}}{(dN/dX)_{\text{MgII}}} \frac{\Omega_{\text{HI}}}{\Omega_{\text{MgII}}}, \quad (34)$$

which can be evaluated as a function of redshift.

In what follows, our estimates apply to $W_r \geq 1 \text{ \AA}$ Mg II absorbers. Adopting the collective measurements of Seyfert et al. (2013), Zhu & Ménard (2013), Chen et al. (2017), and Sebastian et al. (2023) for $(dN/dX)_{\text{MgII}}$ over the redshift range $0.3 \leq z \leq 6.5$, and adopting the measurements of Rao et al. (2006), Zafar et al. (2013b,a) for $(dN/dX)_{\text{HI}}$ over the redshift range $0 \leq z \leq 5$, we can estimate the ratio of the comoving path densities in Eq. 34 over a wide range of redshift. Similarly, we combine the Ω_{MgII} measurements for $0.3 \leq z \leq 2$ from this work with those of Sebastian et al. (2023) for $2 \leq z \leq 6.5$ and adopt the fitted curve to Ω_{HI} obtained from the meta-analysis of DLAs and 21-cm absorbers by Péroux & Howk (2020) to estimate the ratio $\Omega_{\text{HI}}/\Omega_{\text{MgII}}$ as a function of redshift.

For $z \simeq 1$, we find that the ratio of the comoving path densities is ~ 0.4 and that the ratio of the mass densities is $\sim 10^{-4}$, and obtain $\langle N_{\text{MgII}} \rangle / \langle N_{\text{HI}} \rangle \simeq 1.6 \times 10^{-6}$. For $z \simeq 5$, we find that the ratios are ~ 4 and $\sim 2 \times 10^{-6}$, respectively, and obtain $\langle N_{\text{MgII}} \rangle / \langle N_{\text{HI}} \rangle \simeq 3.3 \times 10^{-7}$. Rao et al. (2006, see their Fig. 8) show that $\log \langle N_{\text{HI}} \rangle / \text{cm}^{-2} \simeq 21$, which would imply that $\log \langle N_{\text{MgII}} \rangle / \text{cm}^{-2} \simeq 15.2$ at $z = 1$ and $\log \langle N_{\text{MgII}} \rangle / \text{cm}^{-2} \simeq 14.5$ at $z = 5$, an increase of roughly a factor of ~ 5 over the cosmic time spanning this redshift range. This change provides a crude insight into the degree to which the metallicity and ionization conditions of $W_r \geq 1 \text{ \AA}$ Mg II absorbers evolve with cosmic time. This simple exercise would suggest that metallicity is increasing and ionization level may be decreasing such that the mean column density of the population of strong Mg II absorbers increases by a factor of several across Cosmic Noon. It would seem plausible that constraints on the average metallicity evolution of DLAs could be measured using this method if the comoving path density and mass density of the Mg II absorbers applied in the ratios were accurately measured for DLA-selected absorption systems.

Dust can induce reddening on background quasars, the effect of which can be estimated using Ω_{dust} in the Mg II bearing clouds. Ménard & Fukugita (2012) measured Ω_{dust} for $0.5 < z < 2$ Mg II absorbers and concluded that the slow build up of dust with cosmic time was consistent with long-lived Mg II clouds that are continually integrating dust from star formation of their host galaxies. Comparing to our measured Ω_{MgII} , we find the redshift evolution of Ω_{dust} evolves in parallel with Ω_{MgII} with a ratio $\Omega_{\text{dust}}/\Omega_{\text{MgII}} \sim 2-3$. This

constant ratio is consistent with the inferences of [Ménard & Fukugita \(2012\)](#) about the nature of Mg II absorbers.

7. CONCLUSION

We conducted a survey for intervening absorption lines from the Mg II $\lambda\lambda 2796, 2803$ fine-structure doublet across the redshift range $0.3 < z < 2.2$ in 951 background quasar spectra obtained from the Data Release 2 of the Australian Dark Energy Survey (OzDES) [Lidman et al. \(2020\)](#). The spectral resolution ranges from $R \simeq 1400$ to $R \simeq 1700$ and the signal-to-noise ratios of the spectra range from 20–80, with more than half above 40. We detected 337 Mg II absorbers with $W_r \geq 0.3 \text{ \AA}$ at the 50% completeness level. This study comprises the first blind survey of Mg II absorbers conducted solely in the southern hemisphere (below the celestial equator).

We measured the redshift path density, dN/dz , the comoving path density, dN/dX , and the equivalent width distribution, $n(W_r) = dN/dXdW_r$, per unit absorption path per unit equivalent width. We developed a method for estimating the cosmic Mg II mass density from the equivalent widths of the low-resolution Mg II lines. The model is informed by a high-resolution survey of Mg II absorbers for which column densities were measured using Voigt profile decomposition.

We compared the OzDES southern hemisphere measurements of dN/dz , dN/dX , and $n(W_r)$ to those published from comprehensive Mg II surveys in the northern hemisphere across similar redshifts (e.g., [Steidel & Sargent 1992](#); [Nestor et al. 2005](#); [Lundgren et al. 2009](#); [Seyffert et al. 2013](#); [Zhu & Ménard 2013](#); [Raghunathan et al. 2016](#)). We also compared our estimates for Ω_{MgII} to the results of [Mathes et al. \(2017\)](#) and [Codoreanu et al. \(2017\)](#), the latter allowing us to perform a longitudinal study of redshift evolution from $z = 5.5$ to $z = 0.3$.

Our main findings are as follows:

1. For Mg II absorbers in the southern hemisphere, the redshift path density, dN/dz , and the comoving path density, dN/dX , are consistent with the measured values in northern hemisphere surveys (e.g., [Nestor et al. 2005](#); [Zhu & Ménard 2013](#); [Seyffert et al. 2013](#)). For $W_r > 0.6 \text{ \AA}$ and $W_r > 1.0 \text{ \AA}$, dN/dX is flat, suggesting no evolution over the ~ 7 Gyr period following Cosmic Noon.
2. The equivalent width distribution of the Mg II absorbers in the southern hemisphere is well fit by an exponential function with $N_* = 0.76 \pm 0.04$ and $W_* = 0.76 \pm 0.01 \text{ \AA}$. These fitted parameters are consistent with those obtained from well-known northern hemisphere surveys (e.g., [Nestor et al. 2005](#); [Seyffert et al. 2013](#)).
3. We develop a Monte Carlo model to compute the statistical properties of the column densities for Mg II absorbers in low resolution spectra from the rest-frame equivalent widths. We demonstrated that the model is highly successful at reproducing the Mg II column

density distribution function measured from a high-resolution sample. This method can be generalized to other ions observed in low-resolution spectra.

4. Estimation of Mg II column densities from absorber equivalent widths enabled us to compute the mass density, Ω_{MgII} , over $0.3 \leq z \leq 2.2$. We obtained $\Omega_{\text{MgII}} \sim 5 \times 10^{-7}$, roughly a factor of ~ 10 higher than the upper limits of [Mathes et al. \(2017\)](#) over the same redshift range. The OzDES estimate is also roughly a factor of ~ 10 higher than the measurements of [Codoreanu et al. \(2017\)](#) for $2 \leq z \leq 4$, which would indicate a dramatic discontinuity in the evolution immediately following Cosmic Noon. However, the OzDES measurements are consistent with a smooth flattening of the Mg II mass density after Cosmic Noon following the steady increase measured by [Sebastian et al. \(2023\)](#) from $z \sim 6$ to $z \sim 2$.

It is well known that the calculation of the mass density is dominated by the largest column density systems. In a typical high-resolution CIV survey, the path length covered is more than an order of magnitude smaller than that of, for example, the CIV SDSS survey by [Cooksey et al. \(2013\)](#). Because of the steep column density distribution function, the highest column density absorbers are rare, and are likely not captured in the low-resolution surveys. This would bias their value of Ω_{CIV} downward. In the other hand, as discussed by [Cooksey et al. \(2013\)](#), large low-resolution surveys have enough path length to find large column density systems, but the problem is that the column densities cannot be accurately determined from the low resolution spectra. This is the problem we faced with the OzDES survey. We attempted to resolve this problem by using the high-resolution surveys to inform us of the statistical relationship between column density and equivalent width. That we were able to use our model to accurately reproduce the column density distribution function of Mg II absorbers from their equivalent widths provides confidence that our method is robust.

On the other hand, we could test the validity of our method by applying it to a CIV absorbers in the Sloan Digital Sky Survey (SDSS). These absorbers have been observed extensively with high-resolution spectra. The large database of Voigt profile fits and published Ω_{CIV} values (e.g., [Songaila 2001, 2005](#); [Schaye et al. 2003](#); [Danforth & Shull 2008](#); [Becker et al. 2009](#); [Ryan-Weber et al. 2009](#); [Cooksey et al. 2010](#); [D’Odorico et al. 2010, 2013](#); [Simcoe et al. 2011](#); [Boksenberg & Sargent 2015](#); [Díaz et al. 2016](#); [Bosman et al. 2017](#); [Codoreanu et al. 2018](#); [Manuwal et al. 2021](#); [Davies et al. 2023b](#)) would serve as an excellent test of the Monte Carlo method.

This approach would allow us to validate our column density estimation method. It would build confidence that the model could be applied to any ion for which there is a large database of low resolution measurements and suitable (but smaller) high-resolution database to inform the model. As such, the method holds promise for significantly increasing

our ability to build a census of the mass density of the multiple phases and astrophysical environments of the gaseous universe.

ACKNOWLEDGMENTS

The authors thank the anonymous referee for comments that helped improve the clarity of manuscript. Much gratitude to Alma Sebastian for sharing their data prior to pub-

lication and especially for obliging our request to compute the data presented in Figure 12(b) from their survey. A.A. acknowledges support from a Webber Fellowship administered through the Department of Astronomy at New Mexico State University. G.G.K acknowledge the support of the Australian Research Council Centre of Excellence for All Sky Astrophysics in 3 Dimensions (ASTRO 3D), through project number CE170100013.

APPENDIX

A. THE COLUMN DENSITIES MODEL

The total column density of an absorber tends to increase with equivalent width in proportion to the number of Voigt profile components comprising the system (e.g., Petitjean & Bergeron 1990; Churchill et al. 2003; Churchill et al. 2020). There is an element of scatter, however, as the equivalent width depends on the kinematics of the components, and the system-total column density depends on the column densities of the individuals components. Thus, unfortunately, there is no one-to-one relationship; absorbers of a given W_r can have a range of system-total column densities. We therefore employ a statistical approach and estimate the system-total N for a given W_r from the column density distribution function. As shown in Figure 10(b), for the 198 high-resolution Mg II systems with $W_r \geq 0.3 \text{ \AA}$ that were Voigt profile fitted by C20, the system-total column density distribution function is well described by a Schechter function,

$$f(N)dN = \Phi_0 \left(\frac{N}{N_*} \right)^\alpha \exp \left\{ -\frac{N}{N_*} \right\} \frac{dN}{N_*} \quad (\text{A1})$$

for which we obtained $\alpha = -1.16 \pm 0.03$ and $\log(N_*/\text{cm}^{-2}) = 16.97 \pm 0.09$ for the best-fitted parameters. This serves as a global constraint for our model. That is, any ensemble of Monte Carlo realizations of the OzDES science sample must, on average, yield a measured column density distribution function consistent with the parameters we fitted to Eq. A1 for the C20 sample.

However, we must also account for how the column density distribution function depends on W_r . As can be seen in Figure 13(a), all systems with $W_r < 1.0 \text{ \AA}$ in the C20 sample have column densities smaller than the characteristic column density, i.e., $N < N_*$, and thus firmly reside on the power-law portion of the distribution function. We fitted the power-law function $f(N) = \Phi_0 N^\alpha$ to the C20 systems in the range $W_r \in (0.3, 1.0]$ and obtained $\alpha = -1.49 \pm 0.07$. The observed distribution and the fitted function are illustrated in Figure 13(b). For larger equivalent width systems in the range $W_r \in (1.0, 4.0]$, column densities both below and above the characteristic column density, N_* , are represented. Thus, the column densities in this equivalent width range populate both the power-law and the exponential portion of the column density distribution function and are likely consistent with a populations drawn from a Schechter function. As shown in Figure 13(c), we fitted the C20 systems in the range $W_r \in (1.0, 4.0)$ and adopted $\alpha = -1.16 \pm 0.03$ and $\log(N_*/\text{cm}^{-2}) = 16.97 \pm 0.09$.

Furthermore, as can also be seen in Figure 13(a), the minimum, maximum, and range of column densities increases with increasing W_r . For example, systems with $W_r \simeq 0.3 \text{ \AA}$ have column densities in the range $\log(N/\text{cm}^{-2}) \in (12.5, 14.5)$, whereas systems with $W_r \simeq 1.0 \text{ \AA}$ have column densities in the range $\log(N/\text{cm}^{-2}) \in (13.0, 16.0)$, and those with $W_r \geq 1.0 \text{ \AA}$ exhibit $\log(N/\text{cm}^{-2}) > 13.5$ with a rare few as high as $\log(N/\text{cm}^{-2}) > 17$. We parameterized the lower and upper boundaries for N as a function of W_r using simple linear functions of the form, $\log N(W_r) = N_0 + N_1 W_r$. We denote $N_L(W_r)$ as the lower limit of the column density at W_r and $N_U(W_r)$ as the upper limit. Using the data in Figure 13(a), we found $N_0 = 12.64$ and $N_1 = 0.54$ for $N_L(W_r)$ over the full range $W_r \in (0.3, 4.0)$. For the upper limit, we limit the range for our parameterization of $N_U(W_r)$ to $W_r \in (0.3, 1.0]$, the region where the power-law distribution applies. We found $N_0 = 13.44$ and $N_1 = 3.21$. For $W_r \geq 1.0 \text{ \AA}$, we allow $N_L(W_r) = \infty$, as the exponential of the Schechter function provides the rapid decrease in the frequency of systems with $N > N_*$. The green curve in Figure 13(a) represents $N_L(W_r)$, the orange curve represents $N_U(W_r)$, and the horizontal dashed curve represents N_* for the fit illustrated in panel 13(c).

As we describe below, we use Monte Carlo modeling to obtain realizations of the column densities for the OzDES science sample. For $W_r \in (0.3, 1.0] \text{ \AA}$, we draw column densities from the power-law distribution shown in Figure 13(b) in the range $N(W_r) \in (N_L(W_r), N_U(W_r))$ and, for $W_r \in (1.0, 4.0] \text{ \AA}$, we draw from the Schechter distribution shown in Figure 13(c) in the range $N(W_r) \in (N_L(W_r), \infty)$.

A.1. Power-law Regime

For the range $W_r \in (0.3, 1.0]$, we employ a power-law function of the form

$$f(t; \alpha)dt = t^\alpha dt, \quad (\text{A2})$$

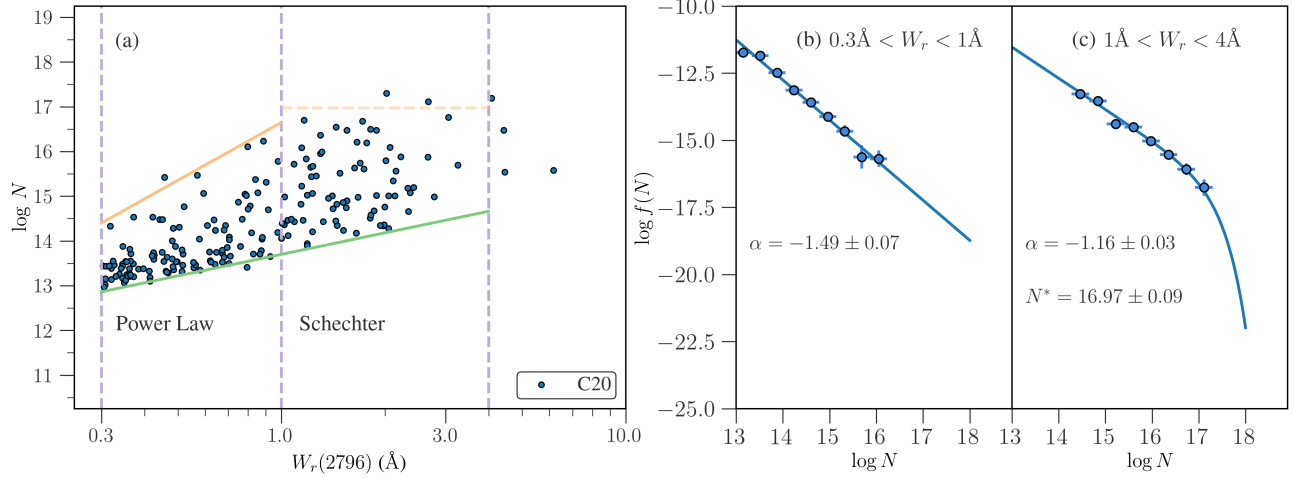


Figure 13. (a) The N – W_r distribution of the **C20** data showing our estimates of the minimum (green line) and maximum (orange line) column density in different W_r ranges. For $W_r \in (0.3, 1.0] \text{\AA}$, the column density distribution is modeled as a power law. For $W_r \in (1.0, 4.0) \text{\AA}$, we model the distribution as a Schechter function with no maximum column density. The horizontal dashed orange line corresponds to the characteristic value, N_* . (b) The column density distribution for $W_r \in (0.3, 1.0] \text{\AA}$. The fit over the range $\log(N/\text{cm}^{-2}) \in (13.1, 15.3)$ yields power-law index $\alpha = -1.49 \pm 0.07$. (c) The column density distribution for $W_r \in (0.6, 1.0] \text{\AA}$. The adopted parameters over the range $\log(N/\text{cm}^{-2}) \in (13.7, 16.2)$ are $\alpha = -1.16 \pm 0.03$ and $\log(N_*/\text{cm}^{-2}) = 16.97 \pm 0.09$.

where α is the power-law slope and t represents the column density. As we show in Figure 13(b), we obtained $\alpha = -1.49 \pm 0.07$ from a power-law fit to the **C20** data for this W_r range. This steeper power-law in this equivalent width regime is an important component of our model, which otherwise overproduced large column densities for smaller W_r systems.

For a given system of W_r in the OzDES sample, we assume that a random deviate, x , corresponds to the fractional area under the column density cumulative distribution function according to

$$x = \frac{\int_{N_L}^N t^\alpha dt}{\int_{N_L}^{N_U} t^\alpha dt} = \frac{N^{\alpha+1} - N_L^{\alpha+1}}{N_U^{\alpha+1} - N_L^{\alpha+1}}, \quad (\text{A3})$$

where $N \in (N_L, N_U)$, where $N_L = N_L(W_r)$ and $N_U = N_U(W_r)$ are the lower and upper ranges to the column density distribution at W_r . To obtain the column density corresponding to a given x , we rearrange Eq. A3, giving

$$N = \left[x (N_U^{\alpha+1} - N_L^{\alpha+1}) + N_L^{\alpha+1} \right]^{1/\alpha+1}. \quad (\text{A4})$$

A.2. Schechter Regime

For the range $W_r \in (1.0, 4.0)$, we employ a Schechter function (Schechter 1976),

$$f(t; \alpha) dt = t^\alpha \exp\{-t\} dt, \quad (\text{A5})$$

where $t = N/N_*$. As we showed in Figure 13(c), we obtained $\alpha = -1.16 \pm 0.03$ and $N_* = 16.97 \pm 0.09$ from a Schechter function fit to the full **C20** sample with $W_r \geq 0.3 \text{\AA}$. For a given a system with a given W_r in the OzDES sample, we assume that a random deviate, x , corresponds to the fractional area under the column density cumulative distribution function according to

$$x = \frac{\int_{t_L}^t t^\alpha \exp\{-t\} dt}{\int_{t_L}^{t_U} t^\alpha \exp\{-t\} dt} = \frac{\Gamma(\alpha-1, t_L) - \Gamma(\alpha-1, t)}{\Gamma(\alpha-1, t_L) - \Gamma(\alpha-1, t_U)}, \quad (\text{A6})$$

where $\Gamma(\alpha-1, t)$ is the incomplete Γ function. Using Brent's method (Brent 1973), we root solve

$$\Gamma(\alpha-1, t) + (x-1)\Gamma(\alpha-1, t_L) - x\Gamma(\alpha-1, t_U) = 0, \quad (\text{A7})$$

for t , from which we obtain $N = N_* t$.

B. ASSESSING THE MODEL

The distribution and median Ω_{MgII} obtained from our Monte Carlo modeling strongly depend on the ability of our model to generate realistic distributions of column densities. To evaluate the degree to which the Monte Carlo model captures the observed distribution of $N-W_r$ pairs of the C20 sample, we performed 10^5 trials using the equivalent widths of the C20 systems. We compared each Monte Carlo realization to the observed distribution presented in Figure 10 using a 2D Kolmogorov–Smirnov (KS) test. We then examined the distribution of the KS-statistic probabilities (p -values) that the null hypothesis is satisfied, where the null hypothesis is that the two distributions are drawn from the same parent population.

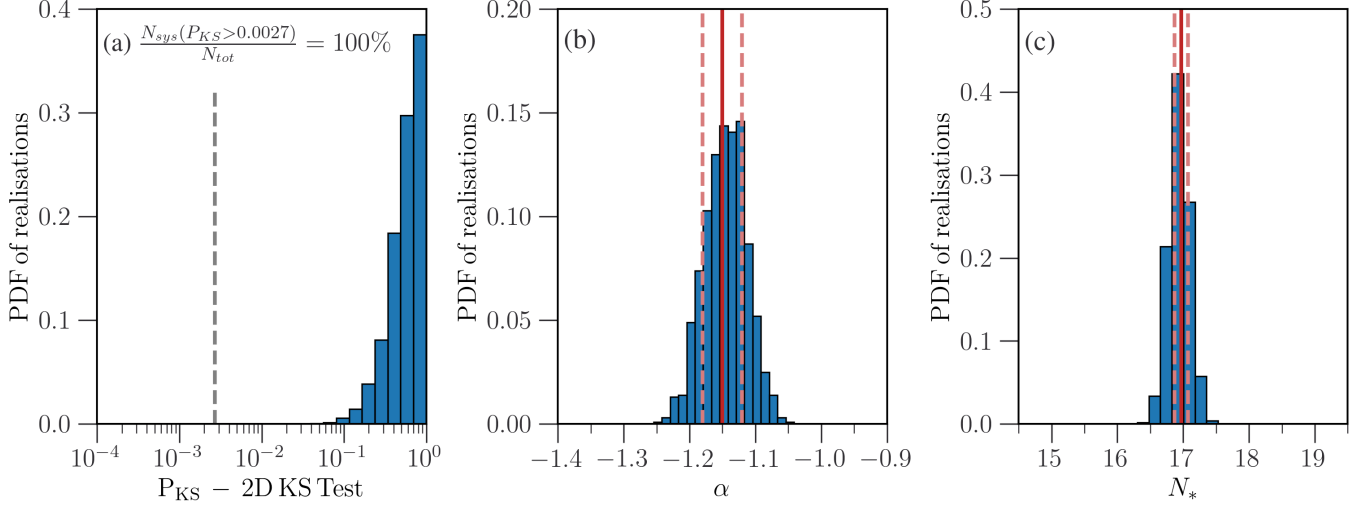


Figure 14. a) The distribution of the 2-dimensional KS p -values obtained by comparing 10^5 Monte Carlo realizations of $N-W_r$ pairs to the observed distribution for the C20 sample (see Figure 10(a)). The black vertical line represents $p = 0.0027$, corresponding to a 99.73% (3σ) confidence level. A p -value less than 0.0027 would suggest that the Monte Carlo realization is not drawn from the same parent population as the C20 sample. No realization yielded $p < 0.0027$. The bulk of the KS tests yield $p > 0.1$, indicating that the Monte Carlo realizations are highly consistent with the C20 sample. (b,c) Distribution of fitted parameters α and N_* of the column density distribution functions for 10^5 realizations of the OzDES science sample. (b) The distribution of Monte Carlo fitted power-law indices (blue histogram) has mean and standard deviation $\alpha = -1.14 \pm 0.05$, which is highly consistent with the measured value $\alpha = -1.16 \pm 0.03$ (red vertical lines) from the C20 sample. (c) The distribution of Monte Carlo fitted characteristic column densities (blue histogram) has mean and standard deviation $\log(N_*/\text{cm}^{-2}) = 16.93 \pm 0.23$, which is highly consistent with the measured value $\log(N_*/\text{cm}^{-2}) = 16.97 \pm 0.09$ (red vertical lines) from the C20 sample.

The distribution of KS p -values from 10^5 Monte Carlo realizations is presented in Figure 14(a). The vertical dashed line shows $p = \text{erf}(3/\sqrt{2}) = 0.0027$. For an individual realization, if $p \leq 0.0027$, we can reject the null hypothesis that the two compared samples are drawn from the same underlying parent population at a confidence level 99.73% (3σ) or higher. We might expect that a non-zero fraction of the 10^5 realizations will have $p \leq 0.0027$. If that fraction is 0.27% (270 realization) or larger, we can reject the null hypothesis for the full suite of Monte Carlo realizations at the 99.73% confidence level or higher. As shown in Figure 14(a), none of the Monte Carlo realizations yielded $p \leq 0.0027$, which suggest we cannot rule out the null hypothesis, i.e., we can conclude that the $N-W_r$ distributions generated by the Monte Carlo model are consistent with the observed distribution of $N-W_r$ pairs of the C20 sample. In fact, the mode of the p -value distribution is $p \simeq 0.85$ and the vast majority of the KS tests yielded $p > 0.1$. The distribution of p -values strongly indicate that our model consistently generates realizations that reflect the observed distribution of $N-W_r$ pairs for the C20 sample.

A second test is to see how well the Monte Carlo realizations recover the column density distribution of the C20 sample, which we measured to have a best-fit power-law slope $\alpha = -1.16 \pm 0.03$ and characteristic column density $\log(N/\text{cm}^{-2}) = 16.97 \pm 0.09$. We generated 10^5 Monte Carlo realizations of the C20 sample. For each realization of the sample, we obtained the best-fit power-law slope and characteristic column density assuming a Schechter function for the column density distribution. In Figure 14(b), we plot the distribution of best-fit α values (blue histogram), which has mean and standard deviation $\alpha = -1.14 \pm 0.05$. The red vertical lines represent the best-fit value and uncertainty from the C20 sample. In Figure 14(c), we plot the distribution of best-fit N_* values (blue histogram), which has mean and standard deviation $\log(N_*/\text{cm}^{-2}) = 16.93 \pm 0.23$. The red vertical lines represent is the best-fit value and uncertainty from the C20 sample. The high degree of consistency between the

mean α and N_* from the Monte Carlo generated column densities and that of the C20 sample strongly suggest that our Monte Carlo realizations accurately reproduce column density distribution functions consistent with observations.

C. THE MASS DENSITY CALCULATION

For a given Monte Carlo realization of the OzDES science sample, the mass density is computed from

$$\Omega_{\text{MgII}}(z) = \frac{H_0}{c} \frac{m_{\text{Mg}}}{\rho_c} \langle N \rangle \frac{dN}{dX}, \quad (\text{C8})$$

where $\langle N \rangle$ is the measured mean column density of the sample of MgII absorbers, and dN/dX is their comoving path density. The product $\langle N \rangle dN/dX$ is equivalent to the total column density per unit of comoving path length. It can be computed using the summation $\langle N \rangle dN/dX = (\sum_i N_i)/\Delta X$, where the sum is taken over all absorbers in a given sample and ΔX is the comoving path length for the sample. Alternatively, since dN/dX is measured for the sample, we can compute (also see Eq. 32)

$$\langle N \rangle \frac{dN}{dX} = \int_{N_L}^{N_U} f(N) N dN, \quad (\text{C9})$$

from the first moment of the column density distribution function, $f(N)$, where N_L and N_U are the minimum and maximum column density for the sample.

For each Monte Carlo realization of the OzDES science sample, we computed α and N_* from a fit to the distribution of column densities generated using the methods describe in Appendix A. To determine the mean column density of the realization, we perform the integral

$$\langle t \rangle = \frac{\int_{t_L}^{\infty} t^{\alpha+1} \exp\{-t\} dt}{\int_{t_L}^{\infty} t^{\alpha} \exp\{-t\} dt} = \frac{\Gamma(\alpha, t_L)}{\Gamma(\alpha-1, t_L)}, \quad (\text{C10})$$

where $t_L = N_L/N_*$ is the minimum and maximum column densities for the realization. We obtain $\langle N \rangle$ for the realization from $\langle t \rangle = \langle N \rangle/N_*$.

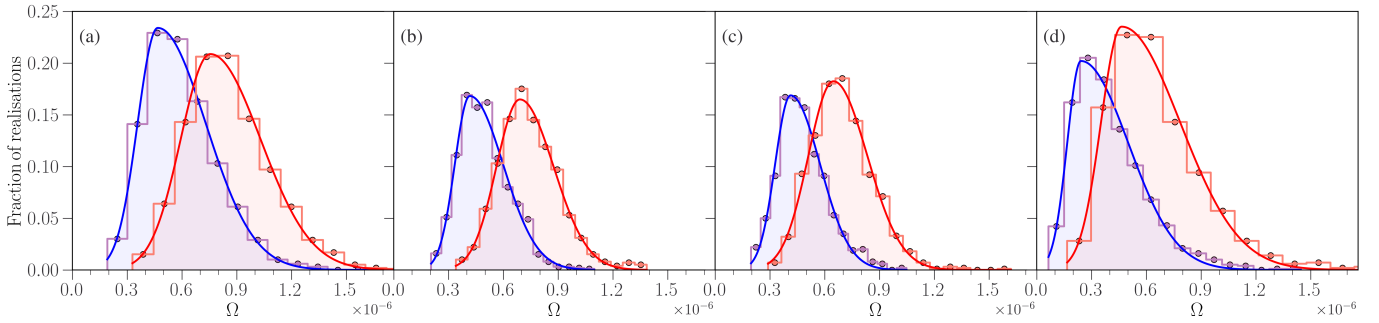


Figure 15. The binned distribution of Ω_{MgII} for the OzDES science sample from the Monte Carlo modeling for four redshift ranges. Both the summation method (purple) and the integral method (red) are shown. (a) $z \in (0.33, 0.80]$. (b) $z \in (0.80, 1.30]$. (c) $z \in (1.30, 1.80]$. (d) $z \in (1.80, 2.20]$. The quoted best values and their uncertainties are determined by fitting univariate asymmetric Gaussians (see Eq. C11). The fits are shown by the curves through the binned distributions. The quoted values (see Eq. C12) are presented in in Table 3 and Figure 11.

We then compute Ω_{MgII} for the realization using Eq. 29 (also see Eq. C8) employing both the summation (Eq. 31) and integral (Eqs. 32, also see Eq. C9) methods. In this way we have two estimates for Ω_{MgII} for each realization. The quoted best value and its uncertainty was obtained by modeling the Ω_{MgII} distributions using a univariate asymmetric Gaussian function (Kato et al. 2002),

$$f(\Omega; \Omega_0, \sigma, \beta) = \frac{1}{\sqrt{2\pi} \sigma} \frac{2}{(1 + \beta)} \begin{cases} \exp\left[\frac{-(\Omega - \Omega_0)^2}{2\sigma^2}\right] & \Omega > \Omega_0 \\ \exp\left[\frac{-(\Omega - \Omega_0)^2}{2\beta^2\sigma^2}\right] & \Omega \leq \Omega_0, \end{cases} \quad (\text{C11})$$

where Ω_0 is the most probable value, β is the asymmetry parameter, σ represents 34% of the area above Ω_0 , and $\beta\sigma$ represents 34% of the area below Ω_0 . The mass densities are then quoted as

$$\Omega_{\text{MgII}} = \Omega_0^{+\sigma}_{-\beta\sigma}. \quad (\text{C12})$$

In Figure 15, we show the distributions of Ω_{MgII} for 10^5 Monte Carlo realizations of the OzDES science sample. Treating each realization as we would treat the real-world OzDES sample, we examine Ω_{MgII} in four redshift bins for each realization. The purple distributions are for the summation method and the red distributions are for the integral method. The solid curves are the fitted functions given by Eq. C11. The final quoted Ω_{MgII} values are listed in Table 3 and presented in Figure 11.

REFERENCES

- Anand, A., Nelson, D., & Kauffmann, G. 2021, *MNRAS*, 504, 65, doi: [10.1093/mnras/stab871](https://doi.org/10.1093/mnras/stab871)
- Becker, G. D., Rauch, M., & Sargent, W. L. W. 2009, *ApJ*, 698, 1010, doi: [10.1088/0004-637X/698/2/1010](https://doi.org/10.1088/0004-637X/698/2/1010)
- Bergeron, J., & Boisse, P. 1984, *A&A*, 133, 374
- Bergeron, J., & Boissé, P. 1991, *A&A*, 243, 344
- Boksenberg, A., & Sargent, W. L. W. 2015, *ApJS*, 218, 7, doi: [10.1088/0067-0049/218/1/7](https://doi.org/10.1088/0067-0049/218/1/7)
- Bosman, S. E. I., Becker, G. D., Haehnelt, M. G., et al. 2017, *MNRAS*, 470, 1919, doi: [10.1093/mnras/stx1305](https://doi.org/10.1093/mnras/stx1305)
- Bouwens, R. J., Illingworth, G. D., Oesch, P. A., et al. 2015, *ApJ*, 803, 34, doi: [10.1088/0004-637X/803/1/34](https://doi.org/10.1088/0004-637X/803/1/34)
- Bradley, L., Davé, R., Cui, W., Smith, B., & Sorini, D. 2022, arXiv e-prints, arXiv:2203.15055, doi: [10.48550/arXiv.2203.15055](https://doi.org/10.48550/arXiv.2203.15055)
- Brent, R. P. 1973, *Algorithms for Minimization without Derivatives* (Englewood Cliffs, NJ: Prentice-Hall), doi: [ISBN0-13-022335-2](https://doi.org/10.1080/13-022335-2)
- Burbidge, E. M., Smith, H. E., Weymann, R. J., & Williams, R. E. 1977, *ApJ*, 218, 1, doi: [10.1086/155651](https://doi.org/10.1086/155651)
- Carswell, R. F., Hilliard, R. L., Strittmatter, P. A., Taylor, D. J., & Weymann, R. J. 1975, *ApJ*, 196, 351, doi: [10.1086/153418](https://doi.org/10.1086/153418)
- Caulet, A. 1989, *ApJ*, 340, 90, doi: [10.1086/167378](https://doi.org/10.1086/167378)
- Cen, R., & Ostriker, J. P. 1999, *ApJ*, 514, 1, doi: [10.1086/306949](https://doi.org/10.1086/306949)
- Chen, S.-F. S., Simcoe, R. A., Torrey, P., et al. 2017, *ApJ*, 850, 188, doi: [10.3847/1538-4357/aa9707](https://doi.org/10.3847/1538-4357/aa9707)
- Childress, M. J., Lidman, C., Davis, T. M., et al. 2017, *MNRAS*, 472, 273, doi: [10.1093/mnras/stx1872](https://doi.org/10.1093/mnras/stx1872)
- Churchill, C. W., Abbas, A., Kacprzak, G. G., & Nielsen, N. M. 2024, *ApJ*, in preparation. <https://arxiv.org/abs/astro-ph/0105044>
- Churchill, C. W., Evans, J. L., Stemock, B., et al. 2020, *ApJ*, 904, 28, doi: [10.3847/1538-4357/abb34](https://doi.org/10.3847/1538-4357/abb34)
- Churchill, C. W., Rigby, J. R., Charlton, J. C., & Vogt, S. S. 1999, *The Astrophysical Journal Supplement Series*, 120, 51, doi: [10.1086/313168](https://doi.org/10.1086/313168)
- Churchill, C. W., Vander Vliet, J. R., Trujillo-Gomez, S., Kacprzak, G. G., & Klypin, A. 2015, *ApJ*, 802, 10, doi: [10.1088/0004-637X/802/1/10](https://doi.org/10.1088/0004-637X/802/1/10)
- Churchill, C. W., & Vogt, S. S. 2001, *AJ*, 122, 679, doi: [10.1086/321174](https://doi.org/10.1086/321174)
- Churchill, C. W., Vogt, S. S., & Charlton, J. C. 2003, *AJ*, 125, 98, doi: [10.1086/345513](https://doi.org/10.1086/345513)
- Churchill, C. W., Vogt, S. S., & Charlton, J. C. 2003, *The Astronomical Journal*, 125, 98, doi: [10.1086/345513](https://doi.org/10.1086/345513)
- Codoreanu, A., Ryan-Weber, E. V., Crighton, N. H. M., et al. 2017, *MNRAS*, 472, 1023, doi: [10.1093/mnras/stx1985](https://doi.org/10.1093/mnras/stx1985)
- Codoreanu, A., Ryan-Weber, E. V., García, L. Á., et al. 2018, *MNRAS*, 481, 4940, doi: [10.1093/mnras/sty2576](https://doi.org/10.1093/mnras/sty2576)
- Cooksey, K. L., Prochaska, J. X., Thom, C., & Chen, H.-W. 2011, *ApJ*, 729, 87, doi: [10.1088/0004-637X/729/2/87](https://doi.org/10.1088/0004-637X/729/2/87)
- Cooksey, K. L., Thom, C., Prochaska, J. X., & Chen, H.-W. 2010, *ApJ*, 708, 868, doi: [10.1088/0004-637X/708/1/868](https://doi.org/10.1088/0004-637X/708/1/868)
- Cooksey, K. L., Kao, M. M., Simcoe, R. A., et al. 2013, *ApJ*, 763, 37, doi: [10.1088/0004-637X/763/1/37](https://doi.org/10.1088/0004-637X/763/1/37)
- Crighton, N. H. M., Murphy, M. T., Prochaska, J. X., et al. 2015, *MNRAS*, 452, 217, doi: [10.1093/mnras/stv1182](https://doi.org/10.1093/mnras/stv1182)
- Croom, S., Saunders, W., & Heald, R. 2004, *Anglo-Australian Observatory Epping Newsletter*, 106, 12
- Danforth, C. W., & Shull, J. M. 2008, *ApJ*, 679, 194, doi: [10.1086/587127](https://doi.org/10.1086/587127)
- Davies, R. L., Ryan-Weber, E., D’Odorico, V., et al. 2023a, *MNRAS*, 521, 289, doi: [10.1093/mnras/stac3662](https://doi.org/10.1093/mnras/stac3662)
- . 2023b, *MNRAS*, 521, 314, doi: [10.1093/mnras/stad294](https://doi.org/10.1093/mnras/stad294)
- Díaz, C. G., Ryan-Weber, E. V., Codoreanu, A., Pettini, M., & Madau, P. 2016, *Boletín de la Asociación Argentina de Astronomía La Plata Argentina*, 58, 54
- D’Odorico, V., Calura, F., Cristiani, S., & Viel, M. 2010, *VizieR Online Data Catalog, J/MNRAS/401/2715*
- D’Odorico, V., Cupani, G., Cristiani, S., et al. 2013, *MNRAS*, 435, 1198, doi: [10.1093/mnras/stt1365](https://doi.org/10.1093/mnras/stt1365)
- D’Odorico, V., Finlator, K., Cristiani, S., et al. 2022, *MNRAS*, 512, 2389, doi: [10.1093/mnras/stac545](https://doi.org/10.1093/mnras/stac545)
- D’Odorico, V., Bañados, E., Becker, G. D., et al. 2023, *MNRAS*, 523, 1399, doi: [10.1093/mnras/stad1468](https://doi.org/10.1093/mnras/stad1468)
- Driver, S. 2021, *Nature Astronomy*, 5, 852, doi: [10.1038/s41550-021-01441-w](https://doi.org/10.1038/s41550-021-01441-w)
- Faucher-Giguère, C.-A. 2020, *MNRAS*, 493, 1614, doi: [10.1093/mnras/staa302](https://doi.org/10.1093/mnras/staa302)
- Flaugher, B. 2005, *International Journal of Modern Physics A*, 20, 3121, doi: [10.1142/S0217751X05025917](https://doi.org/10.1142/S0217751X05025917)
- Förster Schreiber, N. M., & Wuyts, S. 2020, *ARA&A*, 58, 661, doi: [10.1146/annurev-astro-032620-021910](https://doi.org/10.1146/annurev-astro-032620-021910)
- Fumagalli, M., O’Meara, J. M., & Prochaska, J. X. 2016, *MNRAS*, 455, 4100, doi: [10.1093/mnras/stv2616](https://doi.org/10.1093/mnras/stv2616)
- Haardt, F., & Madau, P. 2012, *ApJ*, 746, 125, doi: [10.1088/0004-637X/746/2/125](https://doi.org/10.1088/0004-637X/746/2/125)
- Ho, M.-F., Bird, S., & Garnett, R. 2021, *MNRAS*, 507, 704, doi: [10.1093/mnras/stab2169](https://doi.org/10.1093/mnras/stab2169)

- Jenkins, E. B. 1996, *ApJ*, 471, 292, doi: [10.1086/177969](https://doi.org/10.1086/177969)
- Kacprzak, G. G., & Churchill, C. W. 2011, *MNRAS*, 416, 3118, doi: [10.1111/j.1365-2966.2011.19209.x](https://doi.org/10.1111/j.1365-2966.2011.19209.x)
- Kacprzak, G. G., Churchill, C. W., Ceverino, D., et al. 2010, *ApJ*, 711, 533, doi: [10.1088/0004-637X/711/2/533](https://doi.org/10.1088/0004-637X/711/2/533)
- Kato, T., Omachi, S., & Aso, H. 2002, *Asymmetric Gaussian and Its Application to Pattern Recognition*, *Lecture Notes in Computer Science* (Springer-Verlag Berlin Heidelberg), 405–413, doi: [10.1007/978-94-011-4750-7_11](https://doi.org/10.1007/978-94-011-4750-7_11)
- Khaire, V., & Srianand, R. 2019, *MNRAS*, 484, 4174, doi: [10.1093/mnras/stz174](https://doi.org/10.1093/mnras/stz174)
- Kinman, T. D., & Burbidge, E. M. 1967, *ApJL*, 148, L59, doi: [10.1086/180015](https://doi.org/10.1086/180015)
- Lanzetta, K. M., Turnshek, D. A., & Wolfe, A. M. 1987, *ApJ*, 322, 739, doi: [10.1086/165769](https://doi.org/10.1086/165769)
- Lauroesch, J. T., Truran, J. W., Welty, D. E., & York, D. G. 1996, *PASP*, 108, 641, doi: [10.1086/133780](https://doi.org/10.1086/133780)
- Lehner, N., Koppenhafer, C., O’Meara, J. M., et al. 2022, *ApJ*, 936, 156, doi: [10.3847/1538-4357/ac7400](https://doi.org/10.3847/1538-4357/ac7400)
- Lidman, C., Tucker, B. E., Davis, T. M., et al. 2020, *Monthly Notices of the Royal Astronomical Society*, 496, 19, doi: [10.1093/mnras/staa1341](https://doi.org/10.1093/mnras/staa1341)
- Lundgren, B. F., Brunner, R. J., York, D. G., et al. 2009, *ApJ*, 698, 819, doi: [10.1088/0004-637X/698/1/819](https://doi.org/10.1088/0004-637X/698/1/819)
- Madau, P., & Dickinson, M. 2014, *ARA&A*, 52, 415, doi: [10.1146/annurev-astro-081811-125615](https://doi.org/10.1146/annurev-astro-081811-125615)
- Malik, U., Sharp, R., Penton, A., et al. 2023, *MNRAS*, 520, 2009, doi: [10.1093/mnras/stad145](https://doi.org/10.1093/mnras/stad145)
- Manuwal, A., Narayanan, A., Udhvani, P., et al. 2021, *MNRAS*, 505, 3635, doi: [10.1093/mnras/stab1556](https://doi.org/10.1093/mnras/stab1556)
- Matejek, M. S., Simcoe, R. A., Cooksey, K. L., & Seyffert, E. N. 2013, *ApJ*, 764, 9, doi: [10.1088/0004-637X/764/1/9](https://doi.org/10.1088/0004-637X/764/1/9)
- Mathes, N. L., Churchill, C. W., & Murphy, M. T. 2017, *The Vulture Survey I: Analyzing the Evolution of Mg II Absorbers*. <https://arxiv.org/abs/1701.05624>
- Ménard, B., & Fukugita, M. 2012, *ApJ*, 754, 116, doi: [10.1088/0004-637X/754/2/116](https://doi.org/10.1088/0004-637X/754/2/116)
- Mshar, A. C., Charlton, J. C., Lynch, R. S., Churchill, C., & Kim, T.-S. 2007, *ApJ*, 669, 135, doi: [10.1086/520792](https://doi.org/10.1086/520792)
- Narayanan, A., Misawa, T., Charlton, J. C., & Kim, T.-S. 2007, *ApJ*, 660, 1093, doi: [10.1086/512852](https://doi.org/10.1086/512852)
- Nelson, D., Kauffmann, G., Pillepich, A., et al. 2018, *MNRAS*, 477, 450, doi: [10.1093/mnras/sty656](https://doi.org/10.1093/mnras/sty656)
- Nestor, D. B., Turnshek, D. A., & Rao, S. M. 2005, *The Astrophysical Journal*, 628, 637, doi: [10.1086/427547](https://doi.org/10.1086/427547)
- Newville, M., Stensitzki, T., Allen, D. B., & Ingargiola, A. 2014, *LMFIT: Non-Linear Least-Square Minimization and Curve-Fitting for Python* (Zenodo), doi: [10.5281/zenodo.11813](https://doi.org/10.5281/zenodo.11813)
- Nicastro, F., Kaastra, J., Krongold, Y., et al. 2018, *Nature*, 558, 406, doi: [10.1038/s41586-018-0204-1](https://doi.org/10.1038/s41586-018-0204-1)
- Nielsen, N. M., Churchill, C. W., Kacprzak, G. G., & Murphy, M. T. 2013, *The Astrophysical Journal*, 776, 114, doi: [10.1088/0004-637x/776/2/114](https://doi.org/10.1088/0004-637x/776/2/114)
- Oesch, P. A., Bouwens, R. J., Illingworth, G. D., et al. 2013, *ApJ*, 773, 75, doi: [10.1088/0004-637X/773/1/75](https://doi.org/10.1088/0004-637X/773/1/75)
- . 2014, *ApJ*, 786, 108, doi: [10.1088/0004-637X/786/2/108](https://doi.org/10.1088/0004-637X/786/2/108)
- Oppenheimer, B. D., & Davé, R. 2009, *MNRAS*, 395, 1875, doi: [10.1111/j.1365-2966.2009.14676.x](https://doi.org/10.1111/j.1365-2966.2009.14676.x)
- Penton, A., Malik, U., Davis, T. M., et al. 2022, *MNRAS*, 509, 4008, doi: [10.1093/mnras/stab3027](https://doi.org/10.1093/mnras/stab3027)
- Péroux, C., & Howk, J. C. 2020, *ARA&A*, 58, 363, doi: [10.1146/annurev-astro-021820-120014](https://doi.org/10.1146/annurev-astro-021820-120014)
- Petitjean, P., & Bergeron, J. 1990, *A&A*, 231, 309
- Planck Collaboration. 2020, *Astronomy & Astrophysics*, 641, A6, doi: [10.1051/0004-6361/201833910](https://doi.org/10.1051/0004-6361/201833910)
- Prochter, G. E., Prochaska, J. X., & Bures, S. M. 2006, *ApJ*, 639, 766, doi: [10.1086/499341](https://doi.org/10.1086/499341)
- Raghunathan, S., Clowes, R. G., Campusano, L. E., et al. 2016, *MNRAS*, 463, 2640, doi: [10.1093/mnras/stw2095](https://doi.org/10.1093/mnras/stw2095)
- Rao, S. M., Turnshek, D. A., & Nestor, D. B. 2006, *The Astrophysical Journal*, 636, 610, doi: [10.1086/498132](https://doi.org/10.1086/498132)
- Rao, S. M., Turnshek, D. A., Sardane, G. M., & Monier, E. M. 2017, *MNRAS*, 471, 3428, doi: [10.1093/mnras/stx1787](https://doi.org/10.1093/mnras/stx1787)
- Reddy, N. A., & Steidel, C. C. 2009, *ApJ*, 692, 778, doi: [10.1088/0004-637X/692/1/778](https://doi.org/10.1088/0004-637X/692/1/778)
- Ryan-Weber, E. V., Pettini, M., Madau, P., & Zych, B. J. 2009, *MNRAS*, 395, 1476, doi: [10.1111/j.1365-2966.2009.14618.x](https://doi.org/10.1111/j.1365-2966.2009.14618.x)
- Sargent, W. L. W., Steidel, C. C., & Boksenberg, A. 1988, *ApJ*, 334, 22, doi: [10.1086/166814](https://doi.org/10.1086/166814)
- Savage, B. D., & Sembach, K. R. 1991, *ApJ*, 379, 245, doi: [10.1086/170498](https://doi.org/10.1086/170498)
- Scannapieco, E., Pichon, C., Aracil, B., et al. 2006, *MNRAS*, 365, 615, doi: [10.1111/j.1365-2966.2005.09753.x](https://doi.org/10.1111/j.1365-2966.2005.09753.x)
- Schaye, J., Aguirre, A., Kim, T.-S., et al. 2003, *ApJ*, 596, 768, doi: [10.1086/378044](https://doi.org/10.1086/378044)
- Schechter, P. 1976, *ApJ*, 203, 297, doi: [10.1086/154079](https://doi.org/10.1086/154079)
- Schiminovich, D., Ilbert, O., Arnouts, S., et al. 2005, *ApJL*, 619, L47, doi: [10.1086/427077](https://doi.org/10.1086/427077)
- Schmidt, M. 1963, *Nature*, 197, 1040, doi: [10.1038/1971040a0](https://doi.org/10.1038/1971040a0)
- Schneider, D. P., Hartig, G. F., Jannuzi, B. T., et al. 1993, *ApJS*, 87, 45, doi: [10.1086/191798](https://doi.org/10.1086/191798)
- Schneider, D. P., Richards, G. T., Hall, P. B., et al. 2010, *AJ*, 139, 2360, doi: [10.1088/0004-6256/139/6/2360](https://doi.org/10.1088/0004-6256/139/6/2360)
- Sebastian, A., Ryan-Weber, E. M., Davies, R. L., & Becker, G. D. 2023, *MNRAS*, submitted. <https://arxiv.org/abs/astro-ph/0206497>
- Sembach, K. R., & Savage, B. D. 1992, *The Astrophysical Journal Supplement Series*, 83, 147, doi: [10.1086/191734](https://doi.org/10.1086/191734)
- Seyffert, E. N., Cooksey, K. L., Simcoe, R. A., et al. 2013, *ApJ*, 779, 161, doi: [10.1088/0004-637X/779/2/161](https://doi.org/10.1088/0004-637X/779/2/161)

- Sharp, R., Saunders, W., Smith, G., et al. 2006, in SPIE Proceedings, ed. I. S. McLean & M. Iye (SPIE), doi: [10.1117/12.671022](https://doi.org/10.1117/12.671022)
- Shull, J. M., Danforth, C. W., & Tilton, E. M. 2014, *ApJ*, 796, 49, doi: [10.1088/0004-637X/796/1/49](https://doi.org/10.1088/0004-637X/796/1/49)
- Shull, J. M., Smith, B. D., & Danforth, C. W. 2012, *ApJ*, 759, 23, doi: [10.1088/0004-637X/759/1/23](https://doi.org/10.1088/0004-637X/759/1/23)
- Simcoe, R. A., Cooksey, K. L., Matejek, M., et al. 2011, *ApJ*, 743, 21, doi: [10.1088/0004-637X/743/1/21](https://doi.org/10.1088/0004-637X/743/1/21)
- Songaila, A. 2001, *ApJL*, 561, L153, doi: [10.1086/324761](https://doi.org/10.1086/324761)
- . 2005, *AJ*, 130, 1996, doi: [10.1086/491704](https://doi.org/10.1086/491704)
- Songaila, A., & Cowie, L. L. 2010, *ApJ*, 721, 1448, doi: [10.1088/0004-637X/721/2/1448](https://doi.org/10.1088/0004-637X/721/2/1448)
- Steidel, C. C., Dickinson, M., & Persson, S. E. 1994, *ApJL*, 437, L75, doi: [10.1086/187686](https://doi.org/10.1086/187686)
- Steidel, C. C., & Sargent, W. L. W. 1992, *ApJS*, 80, 1, doi: [10.1086/191660](https://doi.org/10.1086/191660)
- Tripp, T. M., Aracil, B., Bowen, D. V., & Jenkins, E. B. 2006, *ApJL*, 643, L77, doi: [10.1086/505264](https://doi.org/10.1086/505264)
- Tumlinson, J., Peebles, M. S., & Werk, J. K. 2017, *Annual Review of Astronomy and Astrophysics*, 55, 389, doi: [10.1146/annurev-astro-091916-055240](https://doi.org/10.1146/annurev-astro-091916-055240)
- Tytler, D., Boksenberg, A., Sargent, W. L. W., Young, P., & Kunth, D. 1987, *ApJS*, 64, 667, doi: [10.1086/191213](https://doi.org/10.1086/191213)
- Vernet, J., Dekker, H., D’Odorico, S., et al. 2011, *A&A*, 536, A105, doi: [10.1051/0004-6361/201117752](https://doi.org/10.1051/0004-6361/201117752)
- Weymann, R. J., Carswell, R. F., & Smith, M. G. 1981, *Annual Review of Astronomy and Astrophysics*, 19, 41, doi: [10.1146/annurev.aa.19.090181.000353](https://doi.org/10.1146/annurev.aa.19.090181.000353)
- Wolfe, A. M., Turnshek, D. A., Smith, H. E., & Cohen, R. D. 1986, *ApJS*, 61, 249, doi: [10.1086/191114](https://doi.org/10.1086/191114)
- Yu, Z., Martini, P., Penton, A., et al. 2021, *MNRAS*, 507, 3771, doi: [10.1093/mnras/stab2244](https://doi.org/10.1093/mnras/stab2244)
- . 2023, *MNRAS*, 522, 4132, doi: [10.1093/mnras/stad1224](https://doi.org/10.1093/mnras/stad1224)
- Yuan, F., Lidman, C., Davis, T. M., et al. 2015, *MNRAS*, 452, 3047, doi: [10.1093/mnras/stv1507](https://doi.org/10.1093/mnras/stv1507)
- Zafar, T., Péroux, C., Popping, A., et al. 2013a, *A&A*, 556, A141, doi: [10.1051/0004-6361/201321154](https://doi.org/10.1051/0004-6361/201321154)
- Zafar, T., Popping, A., & Péroux, C. 2013b, *A&A*, 556, A140, doi: [10.1051/0004-6361/201321153](https://doi.org/10.1051/0004-6361/201321153)
- Zhu, G., & Ménard, B. 2013, *The Astrophysical Journal*, 770, 130, doi: [10.1088/0004-637x/770/2/130](https://doi.org/10.1088/0004-637x/770/2/130)